NATIONAL TECHNICAL UNIVERSITY OF ATHENS

Joint Postgraduate Course

"Computational Mechanics"

Second-Order Computational Multiscale Homogenization

Postgraduate Dissertation

Ioanna Patitsa

Supervisor: **VISSARION PAPADOPOULOS,** Assistant Professor, NTUA

ATHENS 2015

Ευχαριστίες

Θα ήθελα να εκφράσω τις θερμές και ειλικρινείς ευχαριστίες μου στον επιβλέποντα της εργασίας μου κ. Βησσαρίωνα Παπαδόπουλο , Επ. Καθηγητή του Εργαστηρίου Στατικής και Αντισεισμικών Ερευνών του τομέα Δομοστατικής της Σχολής Πολιτικών Μηχανικών του Εθνικού Μετσόβιου Πολυτεχνείου, για τη δυνατότητα να ασχοληθώ με το αντικείμενο της ομογενοποίησης ,για το ενδιαφέρον και την άμεση ανταπόκριση στις διάφορες απορίες που προέκυπταν καθώς και για την εμπιστοσύνη που μου έδειξε.

Επίσης, θα ήθελα να ευχαριστήσω την υποψήφια διδάκτορα κ. Μαρία Ταβλάκη για τη βοήθειά της.

Τέλος, θα ήθελα να ευχαριστήσω την οικογένειά μου και τους φίλους μου για την αμέριστη συμπαράστασή τους.

Abstract

The aim of this dissertation is the investigation and implementation of the computational multiscale homogenization schemes. To this end, the homogenization solution schemes proposed by [10,12] are used.

Heterogeneous materials are found everywhere. If the heterogeneities are small compared to the scale of the whole problem, a standard finite element analysis often becomes computationally too large. For that reason various homogenization methods have been developed.

Multi-scale computational homogenization is a technique that reduces the amount of calculations, but still manages to capture the heterogeneous properties. It is based on the derivation of the local macroscopic constitutive response from the underlying microstructure through the adequate construction and solution of a microstructural boundary value problem.

First-order computational homogenization schemes fit entirely into a standard local continuum mechanics framework. However, when considering problems of dimensions close to the characteristic length of the material, the size effects can not be neglected and the classical (first-order) multiscale computational homogenization scheme looses accuracy, motivating the use of a second-order multiscale computational homogenization scheme. This second-order scheme uses the classical continuum at the microscale while considering a second-order (i.e. strain gradient) continuum at the macro-scale.

When undertaking conventional displacement-based finite element analysis of second-order continuum, the interpolation of displacements should exhibit at least C^1 continuity. In this dissertation, the structure at macroscale level is discretized by the C^1 two dimensional triangular finite elements, while the C^0 quadrilateral finite element is used for the discretization of the microscale.

The two schemes are implemented in a cantilever beam bending problem. The results are compared.

Key words: computational homogenization, multiscale mechanics, second-order homogenization, C^1 continuity finite element.

Περίληψη

Αντικείμενο της παρούσας μεταπτυχιακής εργασίας είναι η μελέτη και η εφαρμογή των μεθόδων υπολογιστικής ομογενοποίησης πολλαπλών κλιμάκων. Για το σκοπό αυτό, θα χρησιμοποιηθούν οι μέθοδοι υπολογιστικής ομογενοποίησης που έχουν προταθεί από τους [10,12].

Σχεδόν όλα τα βιομηχανικά και τεχνητά υλικά, όπως επίσης και τα φυσικά υλικά, που χαρακτηρίζονται από πολλαπλές κλίμακες, παρουσιάζουν ανομοιογένεια σε κάποια συγκεκριμένη κλίμακα, η οποία έχει σημαντικό αντίκτυπο στην παρατηρούμενη μακροσκοπική συμπεριφορά τους. Η απευθείας αριθμητική επίλυση των προβλημάτων πολλαπλής κλίμακας είναι δύσκολη καθώς απαιτείται ένα τεράστιο ποσό μνήμης του υπολογιστή και μεγάλος χρόνος επεξεργασίας. Για το λόγο αυτό έχουν αναπτυχθεί διάφορες μέθοδοι ομογενοποίησης.

Η υπολογιστική ομογενοποίηση είναι μια τεχνική που ανήκει στην ευρύτερη ομάδα των μεθόδων πολλαπλών κλιμάκων. Βασίζεται ουσιαστικά στον υπολογισμό της τοπικής μακροσκοπικής απόκρισης μέσω ανάλυσης της υποκείμενης μικροδομής με την κατάλληλη κατασκευή και επίλυση ενός προβλήματος συνοριακών τιμών σε επίπεδο μικροκλίμακας.

Η υπολογιστική ομογενοποίηση πρώτης τάξης εφαρμόζεται σε περιπτώσεις που η μακροκλίμακα μπορεί να περιγραφεί με την κλασσική μηχανική συνεχούς μέσου. Ωστόσο, στις εφαρμογές μικρού μεγέθους, η επίδραση της μικροδομής δε μπορεί πια να θεωρηθεί αμελητέα σε σχέση με το μέγεθος του στοιχείου, οδηγώντας έτσι στα, όπως αποκαλούνται, φαινόμενα κλίμακας (size effects). Στις περιπτώσεις αυτές η υπολογιστική ομογενοποίηση πρώτης τάξης χάνει σε ακρίβεια, οδηγώντας έτσι στην απαίτηση ανάπτυξης μιας υπολογιστικής μεθόδου ομογενοποίησης δευτέρας τάξεως.

Στη μέθοδο δευτέρας τάξεως, διατηρείται η θεώρηση του κλασσικού συνεχούς μέσου στη μικροκλίμακα, ενώ στη μακροκλίμακα χρησιμοποιείται μια γενικευμένη θεώρηση συνεχούς μέσου όπου η παραμορφωσιακή ενέργεια, εκτός από την εξάρτηση από τους καθιερωμένους όρους τροπής, εξαρτάται επιπλέον και από τις βαθμίδες τροπής. Στις θεωρίες συνεχούς μέσου τύπου «κλίσεως», εισάγεται συνεπώς η επίδραση της γειτονικής περιοχής σε ένα σημείο.

Στα πλαίσια της κλασικής μεθόδου των πεπερασμένων στοιχείων για την αριθμητική επίλυση προβλημάτων αυτού του είδους απαιτούνται «στοιχεία C^1» που να εξασφαλίζουν συνέχεια της μετατόπισης και των πρώτων χωρικών της παραγώγων. Στην παρούσα εργασία, για την εφαρμογή

της υπολογιστική ομογενοποίηση δευτέρας τάξεως, η μακροκλίμακα διακριτοποιείται με τριγωνικά πεπερασμένα στοιχεία «C^1» ενώ η μικροκλίμακα με τετραπλευρικά ισοπαραμετρικά στοιχεία επίπεδης έντασης.

Οι δύο μέθοδοι (πρώτης –δευτέρας τάξεως) εφαρμόζονται σε ένα πρόβλημα κάμψης δοκού και τα αποτελέσματα συγκρίνονται.

Contents

Chapter 1

Introduction

Heterogeneous materials are found everywhere. Actually, materials that normally are considered homogeneous are heterogeneous on a sufficiently small scale, such as steel. Typical examples include metal alloy systems, porous media, polycrystalline materials and composites. The different phases present in such materials constitute a material microstructure. The size, shape, physical properties and spatial distribution of the microstructural constituents largely determine the macroscopic, overall behaviour of these multi-phase materials.

Consider a problem of various length scales, where the material is heterogeneous on the smallest scale. Solving this problem with a standard finite element analysis requires that the size of the elements correspond with the size of the smallest heterogeneity. For large and complex problems, this leads to a computationally large analysis. To handle this problem in a more efficient way, various techniques have been proposed. A promising approach developed in the recent years is Multi-scale Computational Homogenization. This procedure does not yield closed form over all constitutive equations. Instead it computes stress-strain relations at points of interest on the macroscopic field via a detailed modelling of the microscopic area linked to the point [7].

Computational homogenization introduces a coarser element grid to lower the computational effort. These elements consist themselves of several ordinary finite elements and are named Representative Volume Elements (RVEs), implying that they describe the heterogeneities within their range.

Two independent problems need then to be solved; one microscopic problem and one macroscopic problem. In first and second order computational homogenization, a material will be considered heterogeneous at micro scale and homogeneous at macro scale. The macroscopic behaviour of the material is predicted based on the microscopic properties.

The multiscale analysis using the first-order computational homogenization scheme allows explicit modeling of the microstructure, but retains essential assumptions of the continuum mechanics, and thus gives satisfactory results only for the simple loading cases (tension, pressure, simple shear). It includes only the first gradient of the macroscopic displacement field and it is based on the principles of a local continuum. Therefore, the size effects cannot be captured [12].

Due to the mentioned shortcomings, the first-order computational homogenization scheme has been extended to the second-order computational homogenization framework, where the second-order stress and strain are included. The formulation is based on a non-local continuum theory which takes into account the influence of an environment on the behavior of a material point. Furthermore, the multiscale analysis using the second-order homogenization approach may describe more complex deformation modes, e.g., bending mode. It requires a more complex formulation at the macrolevel (C^1 continuity), which implicates the requirement that both displacements and deformations must be continuous functions. The microlevel in this case can remain on C^0 continuity to keep micro boundary value problem as simple as possible.

1.1 Outline

The aim of this dissertation is the investigation and implementation of the second-order multiscale homogenization scheme.

In chapter 2, the classical first-order computational homogenization in 2D is described, where only the most important aspects regarding the method have been written down. Additionally, some intrinsic limitations of the first-order framework are pointed out.

In chapter 3 the continuum description for the second gradient medium is presented, as in the framework of the second-order computational homogenization a proper description of the macroscopic homogenized continuum is required. Moreover, a finite element computational strategy based on C^1 continuity elements is described.

In chapter 4 the second-order computational homogenization scheme for small strains is presented, as proposed by [12]. The microstructural boundary conditions and the relations for the determination of the averaged stress measures, as well as the extraction of the macroscopic constitutive tangents from the microstructural stiffness are described. The solution scheme of the coupled second-order multiscale computational analysis is outlined.

Chapter 5 presents some illustrative examples of the second-order computational homogenization analysis. A comparison of the performance of the first and second-order techniques is also carried out.

Finally, chapter 6 gives a brief summary of the conclusions

Chapter 2

Computational Homogenization

To model a heterogeneous material in a finite element analysis, the element grid has to be small enough to capture all the material properties in a satisfying way. The problem that can occur in such an analysis is that the calculations become too heavy for the computational machine. One possibility to minimize the computational effort is to make use of multi-scale homogenization. This method divides the problem into two independent problems; a micro scale problem and a macro scale problem. The micro scale problem takes care of the heterogeneities in the material, while the macro scale problem is considered as a homogeneous problem and makes use of average material properties that the micro scale problem results in.

2.1 Assumptions

In computational homogenization the material is assumed to be macroscopically sufficiently homogeneous, but microscopically heterogeneous (the morphology consists of distinguishable components as e.g. inclusions, grains, interfaces, cavities), as illustrated in Fig. 2.1. To make this separation of scales possible, the macroscopic length scale has to be much larger than the microscopic length scale. The microscopic length scale must in turn be much larger than the molecular dimension to be able to describe the properties of the material in a satisfying manner, i.e. $\ell_{molecular} \ll \ell_{micro} \ll \ell_{macro}$ [10].

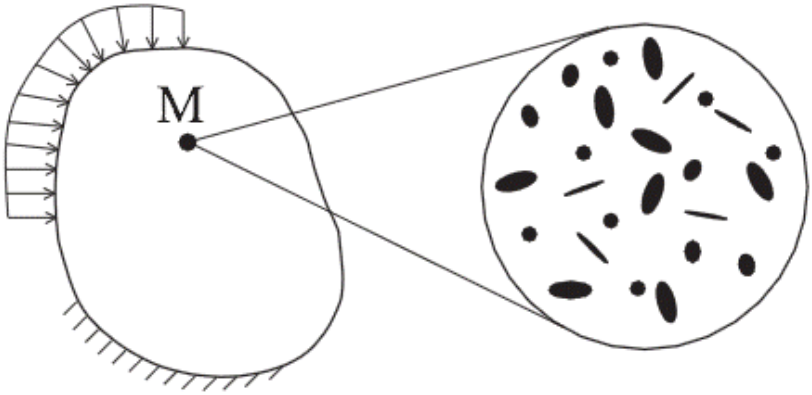

Figure 2.1: Separation of scales [10].

Most of the homogenization approaches make an assumption on global periodicity of the microstructure, suggesting that the whole macroscopic specimen consists of spatially repeated unit cells. In the computational homogenization approach a more realistic assumption on local periodicity is proposed, i.e. the microstructure can have different morphologies corresponding to different macroscopic points, while it repeats itself in a small vicinity of each individual macroscopic point. The concept of local and global periodicity is schematically illustrated in Fig. 2.2

The physical and geometrical properties of the microstructure are identified by a Representative Volume Element (RVE). On macro level the RVEs are considered as points. The actual choice of the RVE is a rather delicate task. The RVE should be large enough to represent the microstructure, without introducing non-existing properties (e.g. undesired anisotropy) and at the same time it should be small enough to allow efficient computational modeling. Since an appropriate RVE has been selected, the properties of the RVEs are used as homogenized properties in the macro scale problem [10].

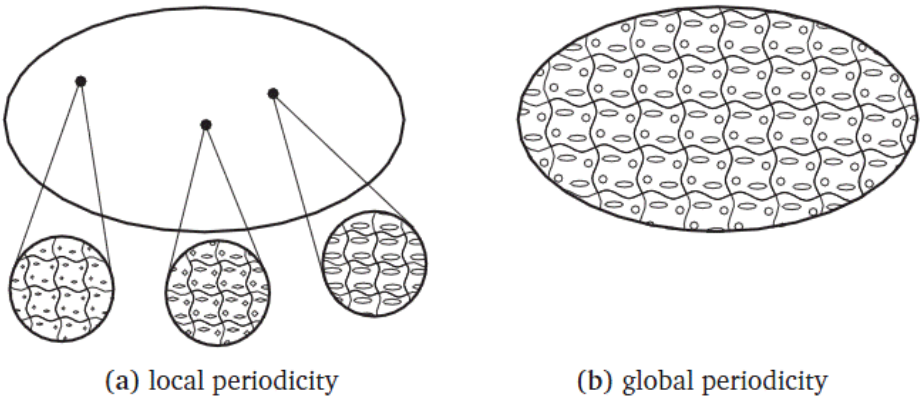

Figure 2.2: Local periodicity compared to global periodicity [10].

2.2 First-order Computational Homogenization

According to the classical formulation of the multi-scale computational homogenization [10,15], two nested boundary value problems are concurrently solved. The initial heterogeneous macroscopic structure is equivalent with a homogeneous one, in each Gauss point of which, a suitably defined RVE is correlated This RVE includes every heterogeneity and non-linearity of the material. With linear or periodic boundary conditions, a macroscopic strain is the loading of the RVE. After analysis and convergence of each RVE in every Gauss point, results concerning the average stress and the stiffness are given back to the macroscopic structure (Fig. 2.3). No assumption for the constitutive law of the macroscopic structure is a priori considered, thus the macroscopic constitutive behavior is numerically obtained. This is a practical solution to the major question of homogenization, namely which are the properties of the homogeneous constitutive law.

Here and in the following the subscript "M" refers to a macroscopic quantity, while the subscript "m" will denote a microscopic quantity.

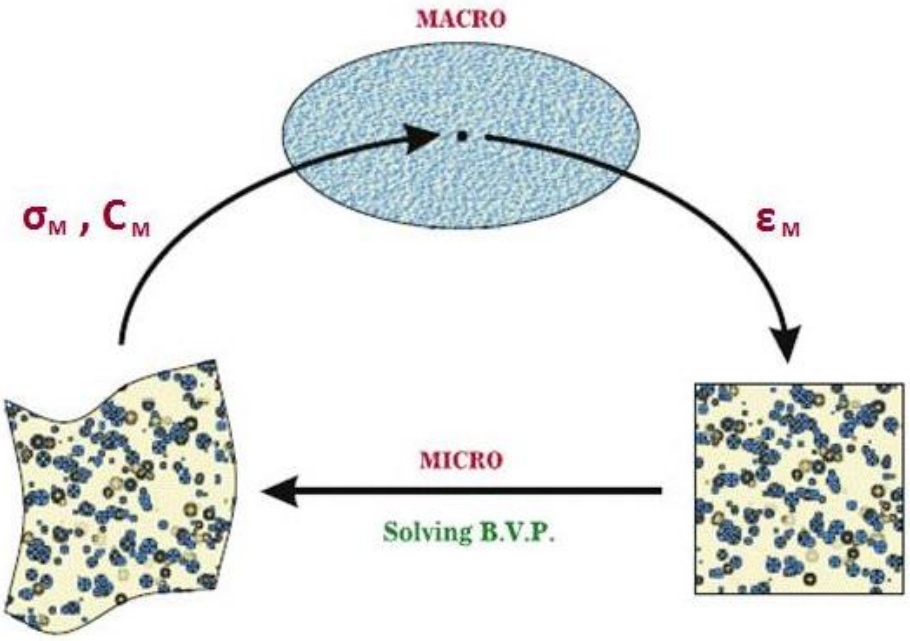

Figure 2.3: First-order computational homogenization scheme [6].

2.2.1 Definition of the problem on the microlevel

The physical and geometrical properties of the microstructure are identified by a representative volume element (RVE). An example of a typical two-dimensional RVE is depicted in Figure 2.4.

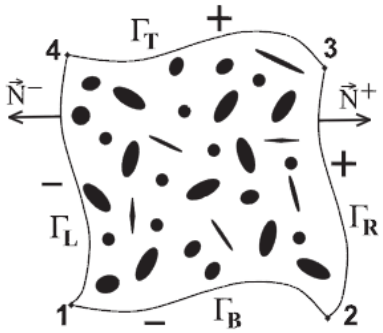

Figure 2.4: Schematic picture of a typical two-dimensional representative volume element (RVE) [10].

The RVE is in a state of equilibrium. This is mathematically reflected by the equilibrium equation in terms of the Cauchy stress tensor $\boldsymbol{\sigma}_m$ according to (in the absence of body forces):

$$\nabla_m \cdot \boldsymbol{\sigma}_m = \vec{0} \text{ in } \Omega_{RVE} \tag{2.1}$$

where Ω_{RVE} is the RVE domain.

2.2.2 Averaging theorems

According to the Hill-Mandel condition or energy averaging theorem, the macroscopic volume average of the variation of work equals to the local work variation, on the RVE:

$$\boldsymbol{\sigma}_\mathbf{M} : \delta\boldsymbol{\varepsilon}_\mathbf{M} = \frac{1}{V_m}\int_{V_m} \boldsymbol{\sigma}_\mathbf{m} : \delta\boldsymbol{\varepsilon}_\mathbf{m} dV_m \tag{2.2}$$

Among others, three widely used types of loading states, which satisfy the above condition, can be applied to the RVE: (a) prescribed linear displacements, (b) prescribed tractions, (c) periodic boundary conditions [4].

According to linear displacement boundary conditions, the loading in the boundaries of the RVE is given by the following relation:

$$\mathbf{u} = \boldsymbol{\varepsilon}_\mathbf{M}\mathbf{x} \qquad \text{at } \mathbf{x} \in \partial V_m \tag{2.3}$$

where a loading strain $\boldsymbol{\varepsilon}_\mathbf{M}$ is applied to the boundaries ∂Vm of the RVE. With **x** is denoted the matrix with the undeformed coordinates of the boundary nodes of the RVE.

Periodic boundary conditions require periodic displacements, as well as antiperiodic tractions, in the opposite boundaries of the RVE. In particular, the displacements of the opposite boundaries are given by the following equations:

$$\begin{aligned} \mathbf{u}_T - \mathbf{u}_B &= \mathbf{u}_4 - \mathbf{u}_1 \\ \mathbf{u}_L - \mathbf{u}_R &= \mathbf{u}_1 - \mathbf{u}_2 \end{aligned} \tag{2.4}$$

where the displacements in the top, bottom, left and right boundary are estimated by using the prescribed displacements of three corner nodes of the RVE, namely 1, 2 and 4, given by relation (2.3).

In order to proceed in the formulation of a homogenization scheme, the average quantities of both the microscopic strain and stress should be defined. The constitutive relation will be then numerically built. The general averaging relations, are:

$$\left\langle \boldsymbol{\varepsilon} \right\rangle_{V_m} = \frac{1}{V_m} \int_{V_m} \boldsymbol{\varepsilon}_m dV_m \tag{2.5}$$

$$\left\langle \boldsymbol{\sigma} \right\rangle_{V_m} = \frac{1}{V_m} \int_{V_m} \boldsymbol{\sigma}_m dV_m \tag{2.6}$$

The equation (2.5) can be further simplified. The volume average microscopic strain is equal to the macroscopic strain which has been applied as loading to the boundaries of the RVE:

$$\left\langle \boldsymbol{\varepsilon} \right\rangle_{V_m} = \boldsymbol{\varepsilon}_M \tag{2.7}$$

In case prescribed displacements are applied to the RVE, the macroscopic stresses is expressed as

$$\left\langle \boldsymbol{\sigma} \right\rangle_{V_m} = \frac{1}{V_m} \mathbf{fx} = \boldsymbol{\sigma}_{\mathrm{M}} \tag{2.8}$$

where **f** is the matrix of the resulting external forces in the undeformed coordinates of the boundary nodes **x** of the RVE, after microscopic analysis has been completed.

A similar relation is applied for the macroscopic stress, in case periodic boundary conditions are used:

$$\langle \boldsymbol{\sigma} \rangle_{V_m} = \frac{1}{V_m} \mathbf{f}_p \mathbf{x}_p = \boldsymbol{\sigma}_{\mathrm{M}} \tag{2.9}$$

where $\mathbf{f}_p$ denotes the external forces in the three corner nodes with prescribed displacements and $\mathbf{x}_p$ the undeformed coordinates of these nodes.

For the completion of the homogenization procedure, the stiffness of the macroscopic structure should be calculated. In particular, the consistent tangent stiffness must be incorporated in the Newton-Raphson incremental iterative procedure. This is obtained numerically, by requiring the relation between the variations of the average microscopic (e.g. the macroscopic) stresses and strains.

2.2.3 Formulation of the multi-scale scheme

The nodes of the RVE mesh are partitioned into those on the surface $\partial\mathcal{V}$ of the RVE and those in the interior [15]. Assume that M < N nodes of the mesh lie on the boundary $\partial\mathcal{V}$. We then consider the partitions of the current nodal positions and internal nodal forces

$$\mathbf{u} = \begin{bmatrix} \mathbf{u}_a \\ \mathbf{u}_b \end{bmatrix} = \begin{bmatrix} \mathbf{P}_a \mathbf{u} \\ \mathbf{P}_b \mathbf{u} \end{bmatrix} \tag{2.10}$$

$$\mathbf{f} = \begin{bmatrix} \mathbf{f}_a \\ \mathbf{f}_b \end{bmatrix} = \begin{bmatrix} \mathbf{P}_a \mathbf{f} \\ \mathbf{P}_b \mathbf{f} \end{bmatrix} \tag{2.11}$$

where $\mathbf{P}_a$ and $\mathbf{P}_b$ are the topological projection matrices, defining internal and boundary contributions, respectively. In line with (2.10), the tangent matrix defined is partitioned as follow:

$$\mathbf{K} = \begin{bmatrix} \mathbf{K}_{aa} & \mathbf{K}_{ab} \\ \mathbf{K}_{ba} & \mathbf{K}_{bb} \end{bmatrix} = \begin{bmatrix} \mathbf{P}_a \mathbf{K} \mathbf{P}_a^{\mathbf{T}} & \mathbf{P}_a \mathbf{K} \mathbf{P}_b^{\mathbf{T}} \\ \mathbf{P}_b \mathbf{K} \mathbf{P}_a^{\mathbf{T}} & \mathbf{P}_b \mathbf{K} \mathbf{P}_b^{\mathbf{T}} \end{bmatrix} \tag{2.12}$$

We examine the case of the prescribed linear displacements on the boundary $\partial\mathcal{V}$ of the RVE. At each node q of this boundary, condition 2.3 induces the discrete constraint

$$\mathbf{u_q} = \boldsymbol{\varepsilon}_\mathbf{M}\mathbf{x_q} \tag{2.13}$$

in terms of the prescribed macroscopic strain $\boldsymbol{\varepsilon}_\mathbf{M}$. Transcribing the strain tensor $\boldsymbol{\varepsilon}_\mathbf{M}$ into vector form, and taking the discretization into consideration, we may rewrite:

$$\mathbf{u}_q = \mathbf{D}_q{}^{\mathbf{T}}\boldsymbol{\varepsilon}_\mathbf{M} \tag{2.14}$$

where $\mathbf{D_q}$ is a matrix that depends on the coordinates of the nodal point q in the reference configuration, for example

$$\mathbf{D}_q = \frac{1}{2}\begin{bmatrix} 2x & 0 & y \\ 0 & 2y & x \end{bmatrix} \tag{2.15}$$

Now define a global coordinate matrix **D** associated with all M nodes on the surface of the discretized microstructure as

$$\mathbf{D} = \left[\mathbf{D}_\mathbf{1}^\mathbf{T}\mathbf{D}_\mathbf{2}^\mathbf{T}\ldots\mathbf{D}_\mathbf{n}^\mathbf{T}\right] \tag{2.16}$$

Then we may rewrite the constraint (2.3) for the linear displacements on the boundary in the compact global form

$$\mathbf{u_b} - \mathbf{D}^\mathbf{T}\boldsymbol{\varepsilon}_\mathbf{M} = \mathbf{0} \tag{2.17}$$

For nonlinear problems the partitioned finite element equation is defined in the incremental form as

$$\begin{bmatrix} \mathbf{K_{aa}} & \mathbf{K_{ab}} \\ \mathbf{K_{ba}} & \mathbf{K_{bb}} \end{bmatrix}\begin{bmatrix} \Delta\mathbf{u_a} \\ \Delta\mathbf{u_b} \end{bmatrix} = \begin{bmatrix} \Delta\mathbf{f_a} \\ \Delta\mathbf{f_b} \end{bmatrix} \tag{2.18}$$

In the convergence state, $\Delta\mathbf{f}_a$ obviously vanishes, which yields

$$\Delta\mathbf{f}_b = \tilde{\mathbf{K}}_{\mathbf{bb}}\Delta\mathbf{u_b} \tag{2.19}$$

where the matrix $\tilde{\mathbf{K}}_{\mathbf{bb}}$ is expressed as

$$\tilde{\mathbf{K}}_{\mathbf{bb}} = \mathbf{K}_{\mathbf{bb}} - \mathbf{K}_{\mathbf{ba}}\mathbf{K}_{\mathbf{aa}}^{-1}\mathbf{K}_{\mathbf{ab}} \tag{2.20}$$

The average stress of the RVE, which is equal to the macro stress, is given by:

$$\Delta\boldsymbol{\sigma}_{\mathbf{M}} = \frac{1}{V}\mathbf{D}\Delta\mathbf{f}_{\mathbf{b}} \tag{2.21}$$

By substitution of Eqs. (2.19) and (2.3) into (2.21), the stress-strain relation is formulated and the consistent tangent stiffness of the macroscopic level, C_M, is obtained:

$$\Delta\boldsymbol{\sigma}_{\mathbf{M}} = \frac{1}{V}\left(\mathbf{D}\tilde{\mathbf{K}}_{\mathbf{bb}}\mathbf{D}^{\mathbf{T}}\Delta\boldsymbol{\varepsilon}_{\mathbf{M}}\right) \tag{2.22}$$

$$\mathbf{C}_{M} = \frac{1}{V}\mathbf{D}\tilde{\mathbf{K}}_{\mathbf{bb}}\mathbf{D}^{\mathbf{T}} \tag{2.23}$$

in terms of the condensed stiffness $\tilde{\mathbf{K}}_{\mathbf{bb}}$.

2.3 The need of second-order scheme

The multiscale analysis using the first-order computational homogenization scheme has been proven to be a versatile tool to establish micromacro structure-property relations in materials, but retains essential assumptions of the continuum mechanics, and thus gives satisfactory results only for the simple loading cases (tension, pressure, simple shear). There are two major disadvantages lying in the existing (first-order) micro-macro computational approaches (as well as the conventional homogenization methods), which significantly limit their applicability. In spite of the fact that these techniques do account for the volume fraction, distribution and morphology of the constituents, they do not incorporate the absolute size of the microstructure, thus making it impossible to address geometrical size effects (Microstructural size effects, which are triggered through small-scale deformation mechanisms, and which can be captured in a local stress-strain response, do not fall into this category.) Another difficulty arises from the

intrinsic assumption of uniformity of the macroscopic (stress or strain) fields attributed to each microstructural representative cell. This uniformity assumption relies on the concept of separation of scales and is not appropriate in critical regions of high deformation gradients, where the macroscopic fields can vary considerably [10].

Due to the mentioned shortcomings, the first-order computational homogenization scheme has been extended to the second-order computational homogenization framework, where the second-order stress and strain are included. The formulation is based on a non-local continuum theory which takes into account the influence of an environment on the behavior of a material point, as proposed by [16,19]. Furthermore, the multiscale analysis using the second-order homogenization approach may describe more complex deformation modes, e.g., bending mode.

Chapter 3

Strain Gradient Material Formulation

3.1 Introduction

Conventional continuum mechanics theories assume that stress at a material point is a function of "state" variables, such as strain, at the same point. This local assumption has long been proved to be adequate when the wavelength of a deformation field is much larger than the dominant micro-structural length scale of the material. However, when the two length scales are comparable, the assumption is questionable as the material behaviour at a point is influenced by the deformation of neighbouring points. Starting from the pioneering Cosserat couple stress theory, various *non-local* or *strain gradient* continuum theories have been proposed. In the full Cosserat theory, an independent rotation quantity **θ** is defined in addition to the material displacement **u**; couple stresses (bending moment per unit area) are introduced as the work conjugate to the micro-curvature (that is, the spatial gradient of **θ**). Later, Toupin [19] and Mindlin [16] proposed a more general theory which includes not only micro-curvature, but also gradients of normal strain. Both the Cosserat and Toupin-Mindlin theories were developed for linear elastic materials. Afterwards, non-local theories for plastic materials have been developed. Interest in non-local continuum plasticity theories has

been rising recently, due to an increasing number of observed size effects in plasticity phenomena [17].

In the present dissertation, the Toupin-Mindlin formulation of strain gradient theory is the base for a finite element implementation for the discretization of the macrostructure in the second-order computational homogenization scheme, as proposed by [8] and [12]. The Toupin-Mindlin formulation furnishes strain gradients and higher order stresses which enter the principle of virtual work as work conjugates.

3.2 Linear Elastic Strain Gradient Theory

Unlike the classical linear elasticity, the grade-2 theories are based on an assumption that strain energy density function is dependent not only on six components of strain but also on the eighteen components of strain gradient. Mindlin [16] proposed a classification of three forms based on different groupings of the eighteen additional arguments of strain energy density function. The strain energy density function having the additional eighteen arguments:

i. Form I: as second gradient of displacement,
ii. Form II: as strain gradient and
iii. Form III: eight components of rotation gradient and ten components of fully symmetric part of second gradient of displacement or strain gradient.

In particular, gradient elasticity which is employed in the present dissertation can be shown as a special case of Form II of Mindlin's theory, i.e. the strain energy density function is expressed as $W = W(\boldsymbol{\varepsilon}_{ij}, \boldsymbol{\varepsilon}_{ij,k})$.

Toupin and Mindlin developed a theory of linear elasticity whereby the strain energy density per unit volume depends upon both strain

$\varepsilon_{ij} = \frac{1}{2}\left(u_{i,j} + u_{j,i}\right)$ and strain gradient η_{ijk}. Here **u** is the displacement field and a comma represents partial differentiation with respect to a Cartesian co-ordinate. Note that $\varepsilon_{ij} = \varepsilon_{ji}$ and $\eta_{ijk} = \eta_{jik}$.

In addition to Cauchy stress σ_{ij} , this theory furnishes higher-order stress $\mu_{ijk}(=\mu_{jik})$ which is work conjugate to the strain gradient η_{ijk}. The local internal work can be expressed as:

$$W = \boldsymbol{\sigma} : \boldsymbol{\varepsilon} + \boldsymbol{\mu} \vdots \boldsymbol{\eta} \tag{3.1}$$

3.2.1 Variational equations of motion

According to the principle of virtual work, variation of strain energy i.e; internal work is equal to the variation of work done by the external forces i.e; external work.

$$\delta W_I = \delta W_E \tag{3.2}$$

where $W_I \int_V W dV$ and W_E is the work done by the external forces.

For the variation of strain energy, the work conjugates of strain and strain gradient are defined as follows:

$$\sigma_{ij} = \frac{\partial W}{\partial \varepsilon_{ij}} = \sigma_{ji} \tag{3.3}$$

$$\mu_{kji} = \frac{\partial W}{\partial \varepsilon_{ij,k}} = \mu_{kij} \tag{3.4}$$

where σ_{ji} , Cauchy stress, is the work conjugate of strain. The first index denotes the plane on which it is acting and the second index denotes the direction of action and μ_{kji} , double stress, is the work conjugate of strain gradient. The first index denotes the plane on which double stress is acting, second index denotes the direction of lever arm and the third index denotes the direction of action. The double stress can be easily appreciated with the help of Figure 3.1.

The variation of strain energy density is

$$\begin{aligned} \delta W &= \frac{\partial W}{\partial \varepsilon_{ij}} \delta \varepsilon_{ij} + \frac{\partial W}{\partial \varepsilon_{ij,k}} \delta \varepsilon_{ij,k} \Rightarrow \\ \delta W &= \sigma_{ji} \delta \varepsilon_{ij} + \mu_{kji} \delta \varepsilon_{ij,k} \end{aligned} \tag{3.5}$$

Using the definition of strain as the symmetric part of displacement gradient, the above equation can be expressed as

$$\delta W = \sigma_{ji} \left(\delta u_{i,j} - \delta \omega_{ij} \right) + \mu_{kji} \left(\delta u_{i,jk} - \delta \omega_{ij,k} \right) \tag{3.6}$$

As σ_{ji} is symmetric and μ_{kji} is symmetric in indices *i* and *j* , we obtain

$$\delta W = \left[\left(\sigma_{ji} - \mu_{kji,k} \right) \delta u_i \right]_{,j} - \left(\sigma_{ji,j} - \mu_{kji,kj} \right) + \left(\mu_{kji} \delta u_{i,j} \right)_{,k} \tag{3.7}$$

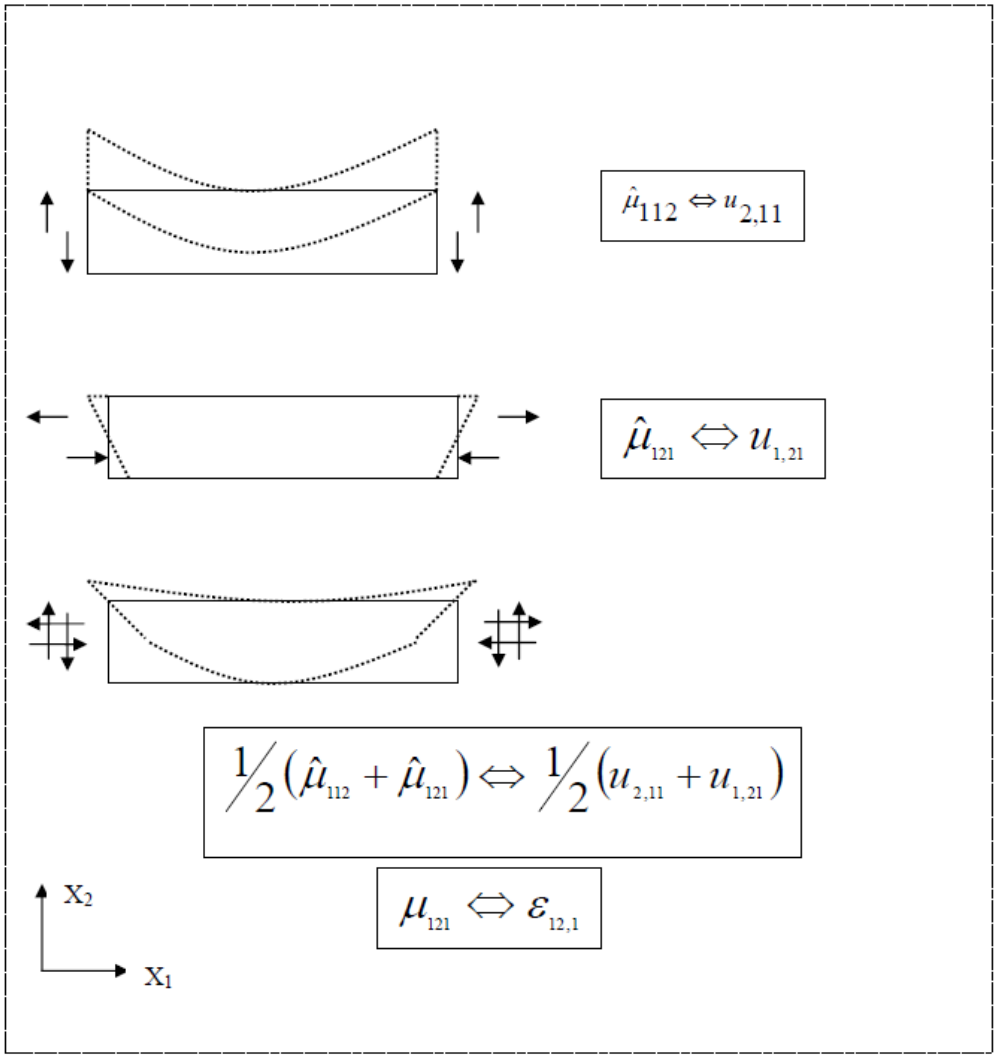

Figure 3.1: Representation of one component of double stress. The ⇔ sign reads as "work conjugate of". As it can be noticed from the figure, double stress is self-equilibrating with no net moment and no net force. The solid line represents the undeformed and dashed line represents the deformed shape [1].

Therefore, the variation of the total strain energy is

$$\delta W_I = \int_V \delta W dV \tag{3.8}$$

Applying divergence theorem to equation (3.8), we obtain

$$\delta W_I = \int_S n_j \left(\sigma_{ji} - \mu_{kji,k}\right)\delta u_i dS - \int_V \left(\sigma_{ji,j} - \mu_{kji,kj}\right)\delta u_i dV + \int_S n_k \mu_{kji}\delta u_{i,j} dS$$

In the last surface integral, the variation of $u_{i,j}$ is not independent of variation of u_i on the surface. As the variation normal derivative of displacement $n_j u_{i,j}$ is independent of variation of displacement u_i on the surface, $u_{i,j}$ in the last integral can be resolved on the boundary into surface gradient and a normal gradient as follows:

$$n_k \mu_{kji}\delta u_{i,j} = n_k \mu_{kji} D_j \delta u_{i,j} + n_k \mu_{kji} n_j D\delta u_{i,j} \tag{3.9}$$

where the operators D_j and D are defined as:

$$D_j = \left(\delta_{jl} - n_j n_l\right)\partial_l \tag{3.10}$$

$$D = n_l \partial_l \tag{3.11}$$

with δ_{jl} being the kroneker delta and ∂_l denotes the spatial partial derivative with respect to the subscript.

The first term on the right hand side of equation (3.9) contains the non-independent variation $D_j\delta u_i$ which can further be expressed as [using the product rule of differentiation (d(u) = d(uv)-d(v))]

$$n_k \mu_{kji} D_j \delta u_i = D_j(n_k \mu_{kji}\delta u_i) + D_j(n_k \mu_{kji})\delta u_i \tag{3.12}$$

The last term in the above equation (3.12) now contains the independent variation of δu_i.

Using the surface divergence theorem, the first term of the equation (3.12) can be written as:

$$D_j(n_k \mu_{kji}\delta u_i) = (D_l n_l) n_j n_k \mu_{kji}\delta u_i \tag{3.13}$$

Assembling all the results from (3.9) to (3.13), equation (3.8) can be written as

$$\delta W_I = \int_S \left[n_j \left(\sigma_{ji} - \mu_{kji,k} \right) - D_j (n_k \mu_{kji}) + (D_l n_l) n_j n_k \mu_{kji} \right] \delta u_i dS -$$
$$- \int_V \left(\sigma_{ji,j} - \mu_{kji,kj} \right) \delta u_i dV + \int_S n_k \mu_{kji} n_j D \delta u_i dS \qquad (3.14)$$

The variation of work done by the external forces, neglecting the body forces, is

$$\delta W_E = \int_S t_i \delta u_i dS + \int_S T_i D \delta u_i dS \qquad (3.15)$$

where **t** and **T** are traction and double traction applied on the surfacere spectively.

For any independent variations of u_i and $D\delta u_i$, the principle of virtual work (equation 3.2) results (for a body of volume *V* and surface *Γ* with normal **n**) in following stress-equilibrium equations

$$div[\hat{\boldsymbol{\sigma}}] = \mathbf{0} \qquad in\ V \qquad (3.16)$$

where the real stress $\hat{\boldsymbol{\sigma}}$ is defined as

$$\hat{\boldsymbol{\sigma}} = \boldsymbol{\sigma} - div[\boldsymbol{\mu}] \qquad (3.17)$$

and boundary conditions are

$$t_i = n_j \left(\sigma_{ji} - \mu_{kji,k} \right) - D_j (n_k \mu_{kji}) + (D_l n_l) n_j n_k \mu_{kji} \qquad (3.18)$$

$$T_i = n_j n_k \mu_{kji} \qquad (3.19)$$

3.3 Finite Element Implementation

When undertaking conventional displacement-based finite element analysis of second-order (i.e. strain gradient) continua, the interpolation of displacements should exhibit at least C^1 continuity, as the virtual work statement includes the first- and second-order derivatives of the displacement. However, due to the complex formulation and practical difficulties associated with the implementation of such elements, the use of mixed C^0 continuous elements is also proposed by many authors [8,10].

In this dissertation, the higher order continuum theory has been implemented , as it has been proposed by [12], into a C^1 triangular finite element already used for the gradient elasticity in [20], in linear elastic fracture mechanics [2], and for the plate bending problem in [3].

3.3.1 C^1 finite element

The finite element used in the present work is a higher-order triangular bending element formulated by Dasgupta & Sengupta [3]. The C^1 finite element is shown in the Fig. 3.2 below.

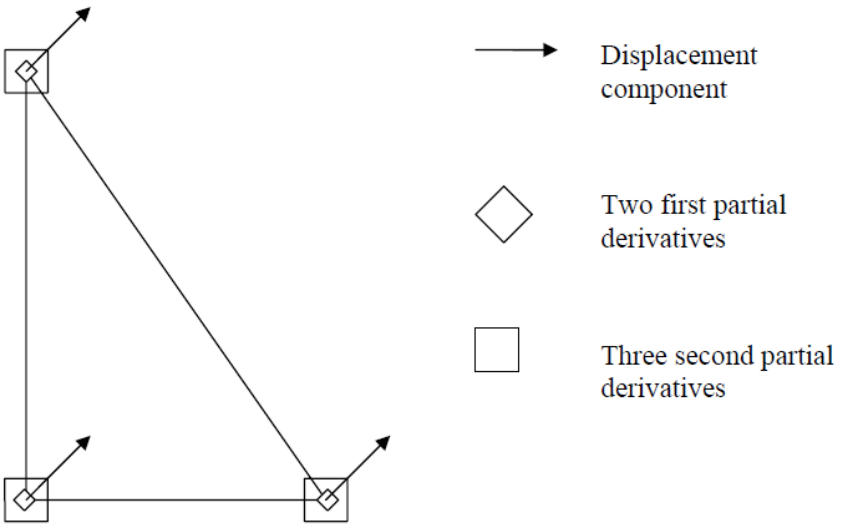

Figure 3.2: C^1 triangular finite element [1].

This element uses a complete quintic polynomial to interpolate displacement field. It has 3 nodes with 6 degrees of freedom per node for each displacement component. The degrees of freedom are the displacement, its two first derivatives and its three second derivatives at each node. This results in eighteen degrees of freedom for each displacement component per each element. Therefore, for the displacement vector field, the total number of degrees of freedom per element is thirty six (36). The normal derivative of displacement along the element edge is constrained to vary as a cubic polynomial. The laplacian of strains vary as quadratic function inside the element [1].

So, the displacement vector is interpolated as follow:

$$\mathbf{u} = \begin{Bmatrix} u \\ v \end{Bmatrix} = [N] \cdot \{\hat{u}\} \tag{3.20}$$

where

$$N = \begin{bmatrix} N_1 \ldots & N_6 & 0 \ldots & 0 & N_7 \ldots & N_{12} & 0 \ldots & 0 & N_{13} \ldots & N_{18} & 0 \ldots & 0 \\ 0 \ldots & 0 & N_1 \ldots & N_6 & 0 \ldots & 0 & N_7 \ldots & N_{12} & 0 \ldots & 0 & N_{13} \ldots & N_{18} \end{bmatrix}$$

and

$$\hat{u} = [u_1 \quad u_{1,x} \quad u_{1,y} \quad u_{1,xx} \quad u_{1,xy} \quad u_{1,yy} \quad v_1 \ldots \quad v_{1,yy} \quad u_2 \ldots \quad u_{2,yy} \quad v_2 \ldots \quad v_{2,yy} \quad u_3 \ldots \quad v_{3,yy}]^T$$

where **u** is the displacement component along the global x-axis and **v** is the displacement component along the global y-axis. N is the matrix of shape functions. The shape functions of this element are given in the Appendix A.

3.3.2 Implementation

The element equations are derived from the variation of the principle of virtual work, which may be expressed for strain gradient continuum as

$$\int_A \delta\boldsymbol{\varepsilon}^{\mathrm{T}}\boldsymbol{\sigma}dA+\int_A \delta\boldsymbol{\eta}^{\mathrm{T}}\boldsymbol{\mu}dA=\int_S \delta\mathbf{u}^{\mathrm{T}}\mathbf{t}ds+\int_S \delta(grad\mathbf{u}^{\mathrm{T}})\mathbf{T}ds \quad (3.21)$$

In Eq. (3.21) **T** is the double traction tensor, **T** = **τn**. *A* and *S* represent the area and the perimeter of the triangle, respectively. The displacement gradients can be derived as

$$\boldsymbol{\varepsilon}=\begin{bmatrix}\varepsilon_{11}\\ \varepsilon_{22}\\ 2\varepsilon_{12}\end{bmatrix}=$$

$$\boldsymbol{\eta}=\begin{bmatrix}\eta_{111}\\ \eta_{222}\\ \eta_{221}\\ \eta_{122}\\ 2\eta_{121}\\ 2\eta_{212}\end{bmatrix}=\mathbf{B}_{\eta}\cdot\{\hat{u}\} \quad (3.22)$$

where $\mathbf{B}_{\boldsymbol{\varepsilon}}$ and $\mathbf{B}_{\boldsymbol{\eta}}$ are the matrices containing corresponding the first and second derivatives of the interpolation functions **N**.

Since a nonlinear problem should be solved, Eq. (3.21) is transformed into the incremental form in the interval (t^{i-1}, t), where t^{i-1} represents the time increment of the last converged equilibrium state, and *t* is the new affine equilibrium state obtained in the iterative procedure using the following relations:

$$\mathbf{u}=\mathbf{u}^{i-1}+\Delta\mathbf{u} \quad (3.23)$$

$$\boldsymbol{\sigma} = \boldsymbol{\sigma}^{i-1} + \Delta\boldsymbol{\sigma}$$

$$\boldsymbol{\mu} = \boldsymbol{\mu}^{i-1} + \Delta\boldsymbol{\mu}$$

Herein $\Delta\mathbf{u}$ denotes the displacement vector increment, while the stress increment $\Delta\boldsymbol{\sigma}$ and the second-order stress increment $\Delta\boldsymbol{\mu}$ are computed by the incremental constitutive relations as

$$\Delta\boldsymbol{\sigma} = \mathbf{C}_{\sigma\varepsilon}\Delta\boldsymbol{\varepsilon} + \mathbf{C}_{\sigma\eta}\Delta\boldsymbol{\eta} \tag{3.24}$$

$$\Delta\boldsymbol{\mu} = \mathbf{C}_{\mu\varepsilon}\Delta\boldsymbol{\varepsilon} + \mathbf{C}_{\mu\eta}\Delta\boldsymbol{\eta} \tag{3.25}$$

where $\mathbf{C}_{\sigma\varepsilon}$, $\mathbf{C}_{\sigma\eta}$, $\mathbf{C}_{\mu\varepsilon}$, $\mathbf{C}_{\mu\eta}$ are the material tangent stiffness matrices. By use of Eq. (3.22), the strain and the second-order strain increments can be expressed in terms of the nodal displacement vector increment $\Delta\hat{\mathbf{u}}$ by the relations

$$\Delta\boldsymbol{\varepsilon} = \mathbf{B}_{\varepsilon}\Delta\hat{\mathbf{u}} \tag{3.26}$$

$$\Delta\boldsymbol{\eta} = \mathbf{B}_{\eta}\Delta\hat{\mathbf{u}}$$

Substituting Eqs. (3.22)–(3.26) into Eq. (3.21), the following finite element relation is obtained

$$\begin{aligned}\left[\int_A (\mathbf{B}_{\varepsilon}^{\mathrm{T}}\mathbf{C}_{\sigma\varepsilon}\mathbf{B}_{\varepsilon} + \mathbf{B}_{\varepsilon}^{\mathrm{T}}\mathbf{C}_{\sigma\eta}\mathbf{B}_{\eta} + \mathbf{B}_{\eta}^{\mathrm{T}}\mathbf{C}_{\mu\varepsilon}\mathbf{B}_{\varepsilon} + \mathbf{B}_{\eta}^{\mathrm{T}}\mathbf{C}_{\mu\eta}\mathbf{B}_{\eta})da\right]\Delta\hat{\mathbf{u}} = \\ \int_S (\mathbf{N}^{\mathrm{T}}\mathbf{t} + grad\mathbf{N}^{\mathrm{T}}\mathbf{T})ds - \int_A (\mathbf{B}_{\varepsilon}^{\mathrm{T}}\boldsymbol{\sigma}^{\mathrm{i\text{-}1}} + \mathbf{B}_{\eta}^{\mathrm{T}}\boldsymbol{\mu}^{\mathrm{i\text{-}1}})dA\end{aligned} \tag{3.27}$$

which may be written in the form

$$\mathbf{K}\Delta\hat{\mathbf{u}} = \mathbf{F}_{\mathbf{e}} - \mathbf{F}_{\mathbf{i}} \tag{3.28}$$

with $\mathbf{K}$ as the element stiffness matrix consisting of the following parts

$$\mathbf{K} = \mathbf{K}_{\sigma\varepsilon} + \mathbf{K}_{\sigma\eta} + \mathbf{K}_{\mu\varepsilon} + \mathbf{K}_{\mu\eta} \tag{3.29}$$

where the particular matrices are defined as

$$\mathbf{K}_{\sigma\varepsilon} = \int_A (\mathbf{B}_\varepsilon^{\mathrm{T}} \mathbf{C}_{\sigma\varepsilon} \mathbf{B}_\varepsilon) dA$$

$$\mathbf{K}_{\sigma\eta} = \int_A (\mathbf{B}_\varepsilon^{\mathrm{T}} \mathbf{C}_{\sigma\eta} \mathbf{B}_\eta) dA \tag{3.30}$$

$$\mathbf{K}_{\mu\varepsilon} = \int_A (\mathbf{B}_\eta^{\mathrm{T}} \mathbf{C}_{\mu\varepsilon} \mathbf{B}_\varepsilon) dA$$

$$\mathbf{K}_{\mu\eta} = \int_A (\mathbf{B}_\eta^{\mathrm{T}} \mathbf{C}_{\mu\eta} \mathbf{B}_\eta) dA$$

Furthermore, $\mathbf{F}_e$ and $\mathbf{F}_i$ are the external and internal nodal force vectors, which are expressed by the relations

$$\mathbf{F}_e = \int_S (\mathbf{N}^{\mathrm{T}} \mathbf{t} + grad \mathbf{N}^{\mathrm{T}} \mathbf{T}) ds \tag{3.31}$$

$$\mathbf{F}_i = \int_A (\mathbf{B}_\varepsilon^{\mathrm{T}} \boldsymbol{\sigma}^{\mathrm{i-1}} + \mathbf{B}_\eta^{\mathrm{T}} \boldsymbol{\mu}^{\mathrm{i-1}}) dA \tag{3.32}$$

Chapter 4

Second-Order Computational Homogenization

In this chapter, the second-order computational homogenization scheme is presented, as an extension of the classical first-order computational homogenization scheme for small strains. In the second-order homogenization approach the macroscopic strain **ε** and the strain gradient **η** are imposed on a microstructural representative volume element.

Every microstructural constituent is modelled as a classical continuum. On the macrolevel, however, a full second gradient equilibrium problem appears. From the solution of the underlying microstructural boundary value problem, the macroscopic stress tensor **σ** and the higher-order stress tensor **μ** are derived based on an extension of the Hill-Mandel condition. This automatically delivers the microstructurally based constitutive response of the second gradient macrocontinuum.

.

4.1 Micro-macro algorithm

4.1.1 Scale transition

The following method, proposed by [12] is used to couple two different continua: a classical (first-order) continuum at the microscale (RVE), and a

higher- (second) order continuum at the macroscale. The micro–macro algorithm consists of the two models representing two different levels. The first level represents the macromodel, discretized in this dissertation by the triangular finite elements described in Chapter 3. As the second level, the microstructure is presented by the representative volume element (RVE), here discretized by the C^0 quadrilateral four-node finite elements. The macroscopic quantities are denoted by the subscript "M", while the microscopic values are labeled with the subscript "m". In every macrolevel integration point of the structural mesh, the RVE microanalysis is performed. The macrolevel displacement gradients $\boldsymbol{\varepsilon_M}$ and $\boldsymbol{\eta_M}$ are transformed into the RVE boundary nodal displacements using corresponding boundary conditions. After solving the RVE boundary value problem, the stress $\boldsymbol{\sigma_M}$, the double stress $\boldsymbol{\mu_M}$ and the constitutive matrices $\mathbf{C_M}$ are obtained by a homogenization procedure. The general scheme of the micro–macro algorithm is presented in Fig. 4.1

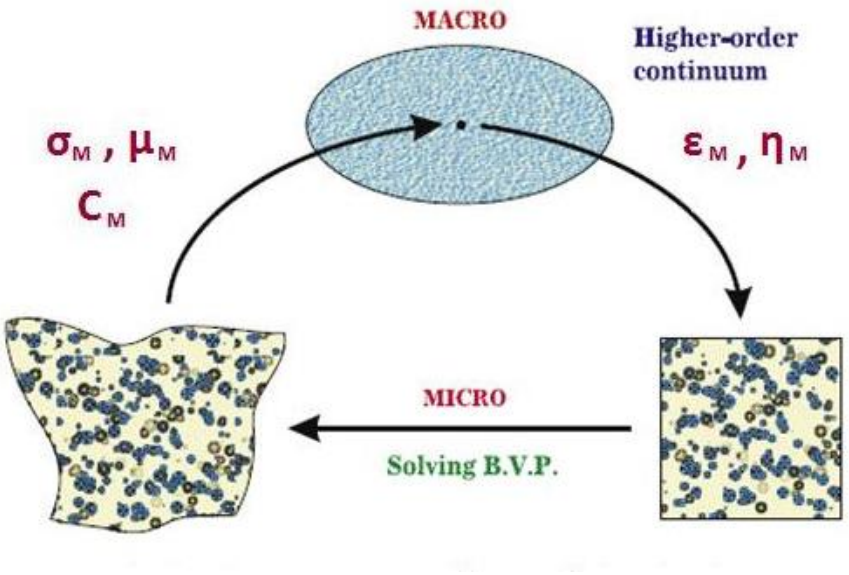

Figure 4.1: Second-order computational homogenization scheme [6].

4.1.2 Downscaling

In the second-order computational homogenization scheme the RVE boundary displacement field is defined by

$$\mathbf{u}_m(\mathbf{X},\mathbf{x}) = \mathbf{u}^0(\mathbf{X}) + \mathbf{x}\cdot\boldsymbol{\varepsilon}_{\mathrm{M}}(\mathbf{X}) + \frac{1}{2}\mathbf{x}\otimes\mathbf{x} : \boldsymbol{\eta}_{\mathrm{M}}(\mathbf{X}) + \mathbf{r}(\mathbf{X},\mathbf{x}) \tag{4.1}$$

where $\mathbf{u}^0(\mathbf{X})$ is the displacement of the macroscopic point to which the RVE is assigned, $\boldsymbol{\varepsilon}_{\mathbf{M}}$ is the macrostrain tensor, $\boldsymbol{\eta}_{\mathbf{M}}$ is the second-order macrostrain tensor, **x** is the fast varying local RVE spatial coordinate, and **X** is the slow varying macroscopic spatial coordinate. The additional term **r** represents the microstructural displacement fluctuation field, which has been added to account for the microscale contribution to the displacement field [8].

In the following, the symmetric operator is dropped (i.e. $\boldsymbol{\varepsilon}$=grad[**u**]) since it has been assumed, for simplicity, that the rotation of the RVE is negligible. Taking the spatial derivative of (4.1) leads to the microscopic strain (microstrain) field within the RVE

$$\begin{aligned} &\boldsymbol{\varepsilon}_m = grad[\mathbf{u}_m] \Rightarrow \\ &\boldsymbol{\varepsilon}_m = \boldsymbol{\varepsilon}_M + \mathbf{x}\cdot\boldsymbol{\eta}_M + grad[\mathbf{r}] \end{aligned} \tag{4.2}$$

The volume average of the microstrain field yields

$$\frac{1}{V}\int_v \boldsymbol{\varepsilon}_m dV = \boldsymbol{\varepsilon}_M + \frac{1}{V}\int_V (\mathbf{x}^T\boldsymbol{\eta}_M) dV + \frac{1}{V}\int_V grad[\mathbf{r}] dV \tag{4.3}$$

where V represents the RVE volume.

In the case that the RVE is centered on the corresponding macroscopic point (i.e. that the local RVE spatial coordinates have their origin at the geometric centre of the RVE), the second term on the right-hand side of (4.3) is automatically zero (first moment of area about the centroid); thus, the microscale fields (**r**, $\boldsymbol{\varepsilon}_{\mathbf{m}}$) can be related to the macrostrain $\boldsymbol{\varepsilon}_{\mathbf{M}}$ only and are not affected by the second-order strain $\boldsymbol{\eta}_{\mathbf{M}}$, as follows:

$$\boldsymbol{\varepsilon}_M = \frac{1}{V}\int_V \boldsymbol{\varepsilon}_m dV - \frac{1}{V}\int_V grad[\mathbf{r}]dV \qquad (4.4)$$

By applying the divergence theorem to the terms on the right-hand side of (4.4) , the relation can also be rewritten in terms of boundary integrals:

$$\boldsymbol{\varepsilon}_M = \frac{1}{V}\int_\Gamma \mathbf{n}\otimes\mathbf{u}d\Gamma - \frac{1}{V}\int_\Gamma \mathbf{n}\otimes\mathbf{r}d\Gamma \qquad (4.5)$$

The volume average of the microstrain $\boldsymbol{\varepsilon}_\mathbf{m}$ needs to be equal to the macrostrain $\boldsymbol{\varepsilon}_\mathbf{M}$; hence, the last integral in both (4.4) and (4.5) must vanish:

$$\frac{1}{V}\int_\Gamma \mathbf{n}\otimes\mathbf{r}d\Gamma = 0 \qquad (4.6)$$

Removing the term associated with $\boldsymbol{\eta}_\mathbf{M}$ from (4.3) by conveniently centering the RVE, has the advantage that higher-order boundary conditions do not have to be prescribed on the RVE. This is consistent with the intention to preserve the microstructural RVE problem as a classical boundary value problem.

Averaging theorems implicit in the first-order computational homogenization scheme have a suitable geometric interpretation—i.e. that both the area and the first moment of area of the deformed RVE (with respect to an arbitrary axis) defined in terms of microscopic displacements are equal to the area and first moment of area of the RVE expressed in terms of macroscopic deformation measures. This assumption consequently places a restriction on the microscopic displacement field which, together with the boundary conditions, leads to a well-posed boundary value problem for deformation of the RVE. In the second-order computational homogenization scheme, it is proposed by [8] to extend this concept, i.e. to include an additional assumption that the second moment of area of the deformed RVE given in terms of microscopic displacements is equal to the second moment of area of the RVE expressed in terms of macroscopic deformation measures.

Following the additional assumption about the second moment of area of the deformed RVE, the relation (4.2) is multiplied by **x** and integrated over the volume *V* of the RVE to give

$$\mathbf{J}\cdot\boldsymbol{\eta}_{\mathrm{M}} = \int_V \mathbf{x}\otimes grad[\mathbf{u}]dV - \int_V \mathbf{x}\otimes grad[\mathbf{r}]dV \qquad (4.7)$$

where $\mathbf{J} = \int_V \mathbf{x}\otimes\mathbf{x}dV$. Once again the centering of the RVE about the macroscopic point has been utilized so that the volume integral of $\mathbf{x}\otimes\boldsymbol{\varepsilon}_{\mathbf{M}}$ conveniently vanishes. Applying the divergence theorem to relation (4.7) gives

$$\mathbf{J}\cdot\boldsymbol{\eta}_{\mathrm{M}} + \frac{1}{2}\mathbf{I}\otimes\mathbf{J}:\boldsymbol{\eta}_{\mathrm{M}} = \int_\Gamma \mathbf{n}\otimes\mathbf{x}\otimes\mathbf{u}d\Gamma - \int_\Gamma \mathbf{n}\otimes\mathbf{x}\otimes\mathbf{r}d\Gamma \qquad (4.8)$$

It should be noted that the relationship between the macroscopic second-order strain (analogous to the reasoning associated with the first-order strain in (4.4)) and the microscopic variables is now given exclusively by integrals over the boundary of the RVE. The additional assumption regarding the second moment of area of the deformed RVE requires that the influence of the displacement fluctuation field should vanish:

$$\int_\Gamma \mathbf{n}\otimes\mathbf{x}\otimes\mathbf{r}d\Gamma = 0 \qquad (4.9)$$

Any RVE boundary conditions used must satisfy relations (4.6) and (4.9). The displacement boundary conditions obey the assumption that **r** = **0**, $\forall\mathbf{x}\in\partial V$, which yields the satisfaction of the two aforementioned relations. The generalized periodic boundary conditions assume identical microfluctuation field on the opposite RVE sides, as defined in Fig. 3, resulting in

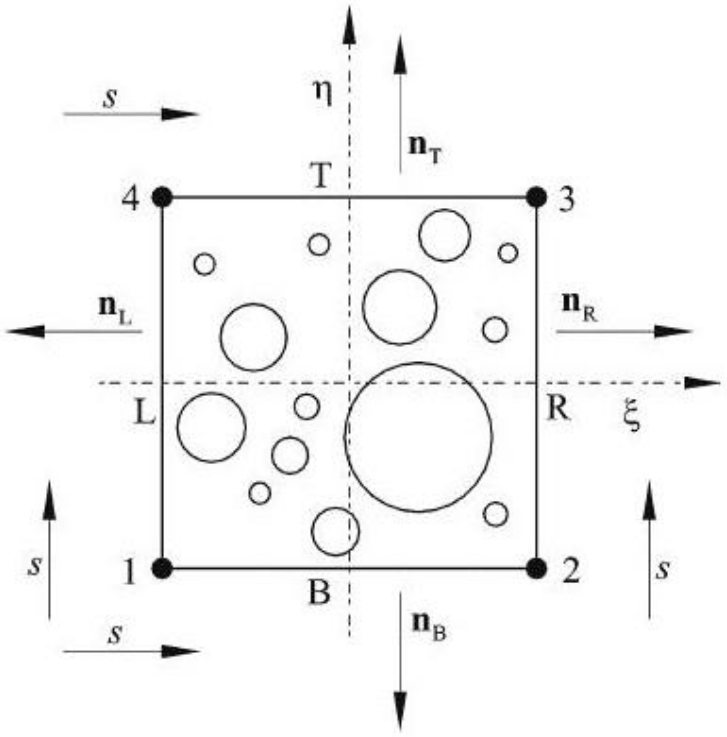

Figure 4.2: Undeformed Representative Volume Element [12].

$$\begin{aligned} \mathbf{r}_L(s) &= \mathbf{r}_R(s) \\ \mathbf{r}_T(s) &= \mathbf{r}_B(s) \end{aligned} \tag{4.10}$$

where *s* is a local coordinate along the edge and the subscripts L, R, T and B stand for the Left, Right, Top and Bottom boundaries of the RVE. From Eq. (4.10), it is obvious that relation (4.6) is satisfied, considering $\mathbf{n}_L$ (s) = $-\mathbf{n}_R$ (s) and $\mathbf{n}_T$ (s) = $-\mathbf{n}_B$ (s). Relation (4.9) is required on two RVE edges only due to the periodicity (4.10). Consequently, relation (4.9) is expressed as

$$\begin{aligned} \int_{A_L} \mathbf{r}_L dA &= 0 \\ \int_{A_B} \mathbf{r}_B dA &= 0 \end{aligned} \tag{4.11}$$

After substituting (4.1) into (4.11), the following expressions are obtained

$$\int_{A_L} \mathbf{u}_L dA = \boldsymbol{\varepsilon}_{\mathrm{M}}^{\mathrm{T}} \int_{A_L} \mathbf{x}_L dA + \frac{1}{2} \boldsymbol{\eta}_{\mathrm{M}} \int_{A_L} (\mathbf{x}_L^T \mathbf{x}_L) dA$$
$$\int_{A_B} \mathbf{u}_B dA = \boldsymbol{\varepsilon}_{\mathrm{M}}^{\mathrm{T}} \int_{A_B} \mathbf{x}_B dA + \frac{1}{2} \boldsymbol{\eta}_{\mathrm{M}} \int_{A_B} (\mathbf{x}_B^T \mathbf{x}_B) dA \tag{4.12}$$

After solving the RVE boundary value problem, the homogenization of the stress tensors and the constitutive matrix has to be carried out [12].

4.1.3 Upscaling

To complete the formulation it is necessary to identify the upscaling of the microstructural response in order to define the macroscopic stress measures in terms of the microscopic quantities. For a statistically homogeneous body, the macroscopic quantities can be defined as the average of the microscopic quantities over the volume of the RVE. According to the Hill–Mandel condition it is required that the local variation of work at a macroscopic point must be equal to the volume average of the variation of work performed on the RVE associated with this macroscopic point:

$$\frac{1}{V} \int_V \left(\delta \boldsymbol{\varepsilon}_{\mathbf{m}}^{\mathbf{T}} \boldsymbol{\sigma}_{\mathbf{m}} \right) dV = \delta \boldsymbol{\varepsilon}_{\mathbf{M}}^{\mathbf{T}} \boldsymbol{\sigma}_{\mathbf{M}} + \delta \boldsymbol{\eta}_{\mathbf{M}}^{\mathbf{T}} \boldsymbol{\mu}_{\mathbf{M}} \tag{4.13}$$

By means of Eq. (4.13), the first-order and the second-order stress tensors are derived in the form of the surface integrals as

$$\boldsymbol{\sigma}_{\mathbf{M}} = \frac{1}{V} \int_\Gamma \left(\mathbf{t}^{\mathbf{T}} \mathbf{x} \right) d\Gamma \tag{4.14}$$

$$\boldsymbol{\mu}_{\mathbf{M}} = \frac{1}{2V} \int_\Gamma \left(\mathbf{x}^{\mathbf{T}} \mathbf{t} \mathbf{x} \right) d\Gamma \tag{4.15}$$

The relations (4.14) and (4.15) can also be transformed into volume integrals, allowing the macroscopic stress measures to be expressed in terms of volume averages of microstructural quantities. The macroscopic stress tensor $\boldsymbol{\sigma}_{\mathrm{M}}$ again equals the volume average of the microscopic stress tensor $\boldsymbol{\sigma}_{\mathrm{m}}$:

$$\boldsymbol{\sigma}_{\mathbf{M}} = \frac{1}{V}\int_{V} \boldsymbol{\sigma}_{\mathbf{m}} dV \tag{4.16}$$

$$\boldsymbol{\mu}_{\mathbf{M}} = \frac{1}{2V}\int_{V} \left(\boldsymbol{\sigma}_{\mathbf{m}}^{\mathbf{T}}\mathbf{x} + \mathbf{x}^{\mathbf{T}}\boldsymbol{\sigma}_{\mathbf{m}}\right) dV \tag{4.17}$$

In the limit case, the infinitesimal force $\mathbf{t}d\Gamma$ in (4.14) and (4.15) tends to $\mathbf{f}_b^i$, representing the nodal force of i_{th} node on the RVE boundary. On the basis of the previous assumption, Eqs. (4.16) and (4.17) transform into

$$\boldsymbol{\sigma}_{\mathbf{M}} = \frac{1}{V}\mathbf{D}\mathbf{f}_{\mathbf{b}} \tag{4.18}$$

$$\boldsymbol{\mu}_{\mathbf{M}} = \frac{1}{V}\mathbf{H}\mathbf{f}_{\mathbf{b}} \tag{4.19}$$

as described by [15]. In Eqs. (4.18) and (4.19) the matrices **D** and **H**, introduced in [8] and [15], are the coordinate matrices involving all the boundary nodes of the RVE. These matrices for the RVE boundary node *i* for the 2D case have the following form

$$\mathbf{D}_i = \frac{1}{2}\begin{bmatrix} 2x & 0 & y \\ 0 & 2y & x \end{bmatrix} \tag{4.20}$$

$$\mathbf{H}_i = \frac{1}{4}\begin{bmatrix} 2x^2 & 0 & 2y^2 & 0 & xy & 0 \\ 0 & 2y^2 & 0 & 2x^2 & 0 & xy \end{bmatrix} \tag{4.21}$$

which are assembled for *n* nodes into the matrices:

$$\mathbf{D} = \left[\mathbf{D}_1^{\mathbf{T}} \mathbf{D}_2^{\mathbf{T}} ... \mathbf{D}_{\mathbf{n}}^{\mathbf{T}} \right] \tag{4.22}$$

$$\mathbf{H} = \left[\mathbf{H}_1^{\mathbf{T}} \mathbf{H}_2^{\mathbf{T}} ... \mathbf{H}_{\mathbf{n}}^{\mathbf{T}} \right] \tag{4.23}$$

In Eqs. (4.18) and (4.19) $\mathbf{f}_b$ is the nodal force vector involving all the boundary nodes on the RVE. Using Eqs. (4.18) and (4.19) the incremental values of the first-order and the second-order stress tensors may be expressed in terms of the boundary nodal forces increment $\Delta\mathbf{f}_b$ as

$$\Delta\boldsymbol{\sigma}_{\mathbf{M}} = \frac{1}{V}\mathbf{D}\Delta\mathbf{f}_{\mathbf{b}} \tag{4.24}$$

$$\Delta\boldsymbol{\mu}_{\mathbf{M}} = \frac{1}{V}\mathbf{H}\Delta\mathbf{f}_{\mathbf{b}} \tag{4.25}$$

According to [10,12,15], the boundary nodal forces can be computed by partitioning RVE algebraic equations. In this setting, the RVE global matrices are transformed into

$$\mathbf{u} = \begin{bmatrix} \mathbf{u}_{\mathbf{a}} \\ \mathbf{u}_{\mathbf{b}} \end{bmatrix} = \begin{bmatrix} \mathbf{P}_{\mathbf{a}}\mathbf{u} \\ \mathbf{P}_{\mathbf{b}}\mathbf{u} \end{bmatrix} \tag{4.26}$$

$$\mathbf{f} = \begin{bmatrix} \mathbf{f}_{\mathbf{a}} \\ \mathbf{f}_{\mathbf{b}} \end{bmatrix} = \begin{bmatrix} \mathbf{P}_{\mathbf{a}}\mathbf{f} \\ \mathbf{P}_{\mathbf{b}}\mathbf{f} \end{bmatrix} \tag{4.27}$$

$$\mathbf{K} = \begin{bmatrix} \mathbf{K}_{\mathbf{aa}} & \mathbf{K}_{\mathbf{ab}} \\ \mathbf{K}_{\mathbf{ba}} & \mathbf{K}_{\mathbf{bb}} \end{bmatrix} = \begin{bmatrix} \mathbf{P}_{\mathbf{a}}\mathbf{K}\mathbf{P}_{\mathbf{a}}^{\mathbf{T}} & \mathbf{P}_{\mathbf{a}}\mathbf{K}\mathbf{P}_{\mathbf{b}}^{\mathbf{T}} \\ \mathbf{P}_{\mathbf{b}}\mathbf{K}\mathbf{P}_{\mathbf{a}}^{\mathbf{T}} & \mathbf{P}_{\mathbf{b}}\mathbf{K}\mathbf{P}_{\mathbf{b}}^{\mathbf{T}} \end{bmatrix} \tag{4.28}$$

where $\mathbf{P}_a$ and $\mathbf{P}_b$ are the topological projection matrices, defining internal and boundary contributions, respectively. For nonlinear problems the partitioned finite element equation is defined in the incremental form as

$$\begin{bmatrix} \mathbf{K}_{aa} & \mathbf{K}_{ab} \\ \mathbf{K}_{ba} & \mathbf{K}_{bb} \end{bmatrix} \begin{bmatrix} \Delta\mathbf{u}_a \\ \Delta\mathbf{u}_b \end{bmatrix} = \begin{bmatrix} \Delta\mathbf{f}_a \\ \Delta\mathbf{f}_b \end{bmatrix} \tag{4.29}$$

In the convergence state, $\Delta\mathbf{f}_a$ obviously vanishes, which yields

$$\Delta\mathbf{f}_b = \tilde{\mathbf{K}}_{bb}\Delta\mathbf{u}_b \tag{4.30}$$

where the matrix $\tilde{\mathbf{K}}_{bb}$ is expressed as

$$\tilde{\mathbf{K}}_{bb} = \mathbf{K}_{bb} - \mathbf{K}_{ba}\mathbf{K}_{aa}^{-1}\mathbf{K}_{ab} \tag{4.31}$$

Hereafter the RVE boundary nodes displacement increment $\Delta\mathbf{u}_b$ is derived by means of Eqs. (4.1), (4.22) and (4.23) resulting in

$$\Delta\mathbf{u}_b = \mathbf{D}^T\Delta\boldsymbol{\varepsilon}_M + \mathbf{H}^T\Delta\boldsymbol{\eta}_M \tag{4.32}$$

Substitution of Eqs. (4.32) and (4.30) into (4.24) and (4.25) yields

$$\Delta\boldsymbol{\sigma}_M = \frac{1}{V}\left(\mathbf{D}\tilde{\mathbf{K}}_{bb}\mathbf{D}^T\Delta\boldsymbol{\varepsilon}_M + \mathbf{D}\tilde{\mathbf{K}}_{bb}\mathbf{H}^T\Delta\boldsymbol{\eta}_M\right) \tag{4.33}$$

$$\Delta\boldsymbol{\mu}_M = \frac{1}{V}\left(\mathbf{H}\tilde{\mathbf{K}}_{bb}\mathbf{D}^T\Delta\boldsymbol{\varepsilon}_M + \mathbf{H}\tilde{\mathbf{K}}_{bb}\mathbf{H}^T\Delta\boldsymbol{\eta}_M\right) \tag{4.34}$$

Finally, comparing Eqs. (4.33) and (4.34) with (3.24) and (3.25), the following identities are easily observed

$$\mathbf{C}_{\sigma\varepsilon} = \frac{1}{V}\mathbf{D}\tilde{\mathbf{K}}_{\mathbf{bb}}\mathbf{D}^{\mathbf{T}}$$

$$\mathbf{C}_{\sigma\eta} = \frac{1}{V}\mathbf{D}\tilde{\mathbf{K}}_{\mathbf{bb}}\mathbf{H}^{\mathbf{T}}$$

(4.35)

$$\mathbf{C}_{\mu\varepsilon} = \frac{1}{V}\mathbf{H}\tilde{\mathbf{K}}_{\mathbf{bb}}\mathbf{D}^{\mathbf{T}}$$

$$\mathbf{C}_{\mu\eta} = \frac{1}{V}\mathbf{H}\tilde{\mathbf{K}}_{\mathbf{bb}}\mathbf{H}^{\mathbf{T}}$$

representing the tangent stiffness matrices at the macrolevel, $\mathbf{C_M}$ [12].

4.2 Nested solution scheme

Summarizing the second-order computational homogenization framework, this section discusses the nested solution scheme for the coupled multi-scale numerical analysis. The structure of the coupled micro-macro program can be outlined as follows [10].

The macroscopic structure to be analyzed is discretized by finite elements. To each macroscopic integration point a unique microstructural RVE is assigned. The geometry and material properties of an RVE are based on the microstructure of the underlying material. The RVE selected should be "representative", i.e. it should contain sufficient information on the microstructural features and basic mechanisms of their interaction.

In order to initiate the macroscopic finite element analysis, constitutive tangents at every integration point are required. To obtain these tangents from the microstructural properties a preparing microstructural analysis is performed. During this initialization the stiffness matrix of an undeformed RVE

is assembled and used to derive the initial macroscopic constitutive tangents at a macroscopic integration point.

During the actual analysis the external macroscopic load is applied in increments. For every step of the macroscopic incremental-iterative procedure, and in each macroscopic integration point, the macrostrain $\boldsymbol{\varepsilon}_M$ and the second-order strain $\boldsymbol{\eta}_M$ are calculated based on the current (iterative) macroscopic displacement field. These values are sent to the microlevel, where they are used to define the boundary value problem for the RVE, corresponding to the respective macroscopic integration point. Upon the solution of every RVE problem, the averaged stress tensor $\boldsymbol{\sigma}_M$ and the second-order stress tensor $\boldsymbol{\mu}_M$ are obtained using (4.18) and (4.19). Additionally, the constitutive tangents are extracted according to (4.35) and returned to the macroscopic program.

When the analysis of all RVEs is finished, the stress tensor, the second-order stress tensor and the consistent constitutive tangents are available at every macroscopic integration point. Hence, macroscopic internal nodal forces can be calculated, higher-order equilibrium can be evaluated and, if required, the next macroscopic iteration can be performed. If equilibrium is achieved the calculations can be continued for the next increment. This solution scheme is summarized in Table 4.1 and in Fig. 4.3.

Obviously, the multi-scale algorithm described above is parallel by its nature. All RVE calculations for one macroscopic iteration can be performed at the same time without any exchange of data between them. So the use of parallel processors for the RVE analyses would significantly reduce the total micro-macro calculation time.

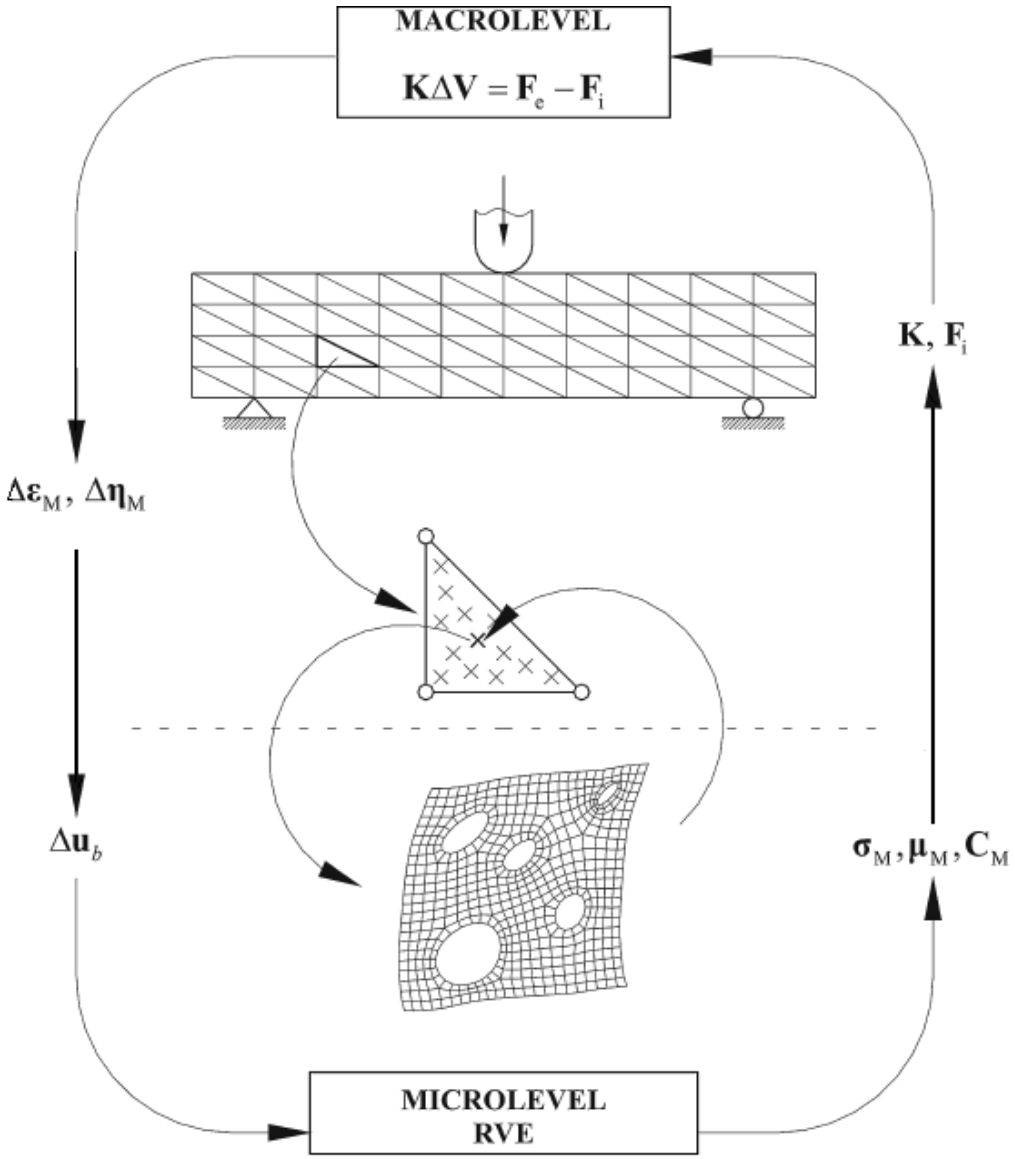

Figure 4.3: Micro-macro algorithm [12].

MACRO		MICRO
1. Initialization ⋆initialize the macroscopic model ⋆ assign an RVE to every integration point ⋆ loop over all integration points Initialization RVE analysis		
for $\boldsymbol{\varepsilon_M^{unit}}$ and $\boldsymbol{\eta_M = 0}$	$\boldsymbol{\varepsilon_M}$ $\boldsymbol{\eta_M}$ →	Initialization RVE analysis ⋆prescribe boundary conditions ⋆assemble the RVE stiffness ⋆calculate the tangents **Cσε Cση Cμε Cμε**
end integration point loop	**tangents** ←	
2. Next increment apply increment of the macro load 3. Next iteration assemble the macroscopic tangent stiffness ⋆solve the macroscopic system ⋆loop over all integration points RVE analysis		RVE analysis
⋆calculate $\boldsymbol{\varepsilon_M}$ and $\boldsymbol{\eta_M}$ = 0	$\boldsymbol{\varepsilon_M}$ $\boldsymbol{\eta_M}$ →	⋆prescribe boundary conditions ⋆assemble the RVE stiffness ⋆solve the RVE problem
	$\boldsymbol{\sigma_M}$ $\boldsymbol{\mu_M}$	⋆calculate σ_M , μ_M ⋆ calculate the tangents **Cσε Cση Cμε Cμε**
⋆ end integration point loop ⋆ assemble the macroscopic internal forces	**tangents** ←	
4. Check for convergence ⋆ if not converged ⇒ step 3 ⋆else ⇒ step 2		

Table 4.1: Incremental-iterative nested multi-scale solution scheme for the second-order computational homogenization.

Chapter 5

Numerical Examples

In the previous chapters the first-order and second-order computational homogenization schemes have been presented. This chapter focuses on the implementation of these two techniques. At first, in section 5.1 RVEs subjected to a given macroscopic deformation are analyzed. The results obtained from the first-order and the second-order computational homogenization modelling are compared and the ability of the second-order scheme to capture gradient effects is demonstrated. In section 5.2 the micro-macro algorithm of the second-order computational homogenization is evaluated by being implemented in a benchmark (pure bending of a homogeneous cantilever beam) problem. Finally, in section 5.3, the first-order and the second-order computational homogenization schemes are compared in a problem of bending of a cantilever beam consisting of a material with embedded fibers.

5.1 Microstructural analysis

In this section, some features of the second order homogenization scheme are illustrated by analyzing a single RVE subjected to a given macroscopic path.

5.1.1 RVE modes of deformation

Firstly, it will be showed how the strain gradient $\boldsymbol{\eta}_M$ affects the deformation of the RVE. According to [13], the deformation modes of an RVE that correspond to particular components of the second gradient tensor are distinguished in four categories of deformation (3D case): extensional, trapezoidal, curvature, and twist named according to their affect on an otherwise undeformed cubic RVE (Fig.5.1).

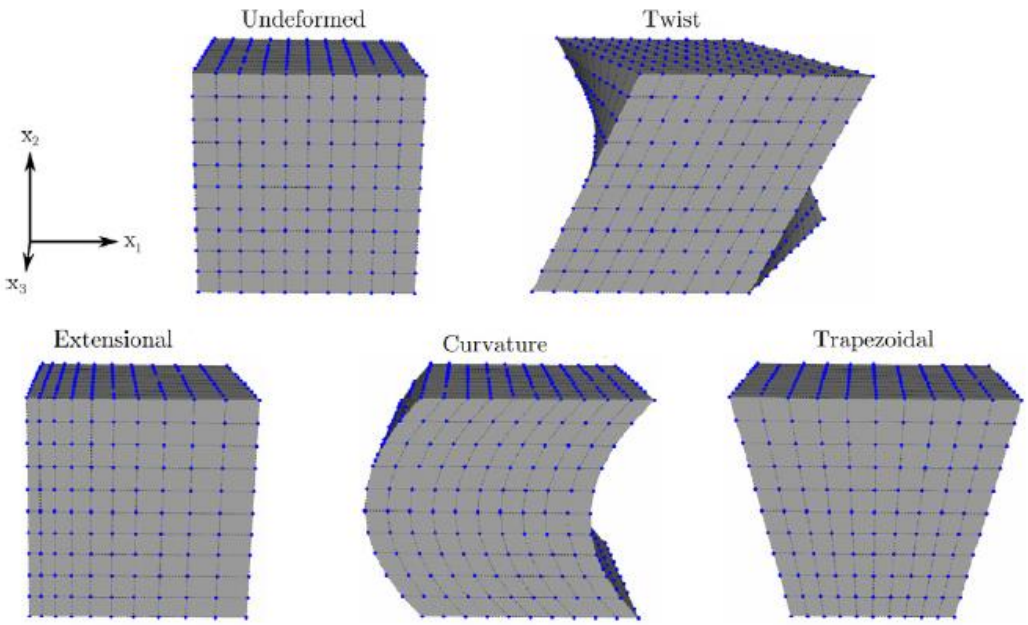

Figure 5.1: Examples of RVE deformation associated with nonzero components of second gradient tensor [13].

We consider a 2D homogeneous RVE model discretized by 4x4 quadrilateral plane stress finite elements (Fig.5.2). When the gradient components of first order strain $\boldsymbol{\varepsilon}_M$ are applied on RVE boundaries, the two well known modes of deformation, stretch and shear, occur. The deformed shape of RVE for $\boldsymbol{\varepsilon}$={0.01 0 0} and $\boldsymbol{\varepsilon}$={0 0 0.01 } are illustrated in Fig 5.3.

The components of strain gradient $\boldsymbol{\eta_M}$ cause three (in 2D case) additional modes of deformation. In Fig 5.4 the deformed shapes are shown for $\eta_{111}=0.02$, $\eta_{221}=0.02$ and $2\eta_{121}=0.02$.

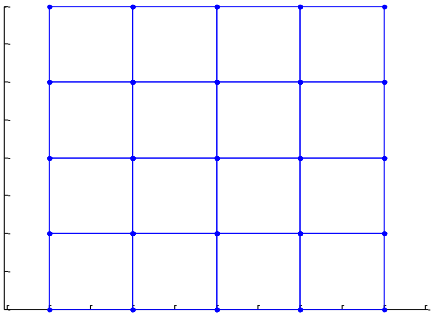

Figure 5.2: Undeformed RVE

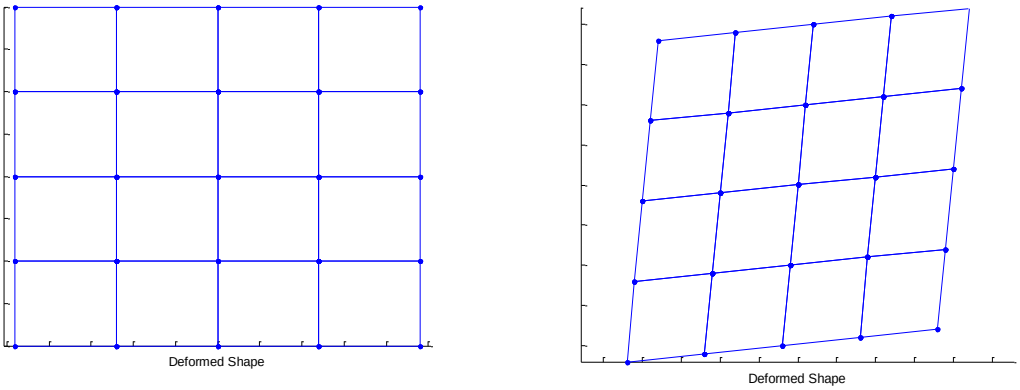

Figure 5.3: RVE deformation associated with nonzero components of $\boldsymbol{\varepsilon_M}$

a) $\varepsilon_{11}=0.01$, b) $2\varepsilon_{12}=0.01$.

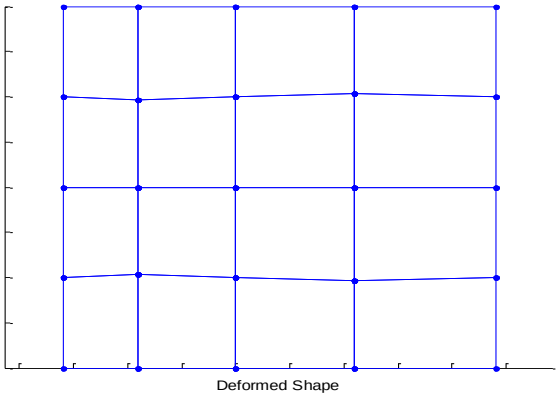

(a)

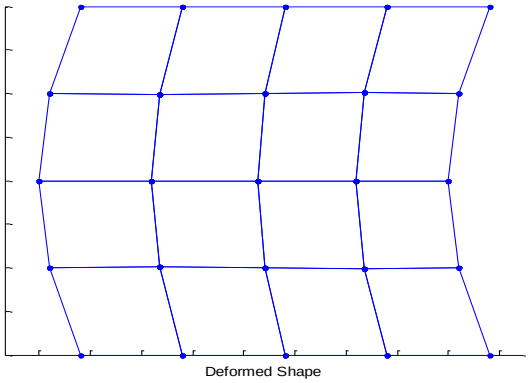

(b)

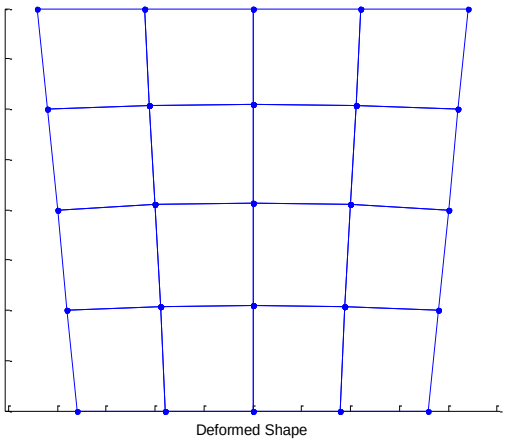

(c)

Figure 5.4: RVE deformation associated with nonzero components of second order strain $\boldsymbol{\eta}_M$ a) $\eta_{111}=0.02$ (Extensional) b) $\eta_{221}=0.02$ (Curvature) c) $2\eta_{121}=0.02$ (Trapezoidal).

5.1.2 Size effects for a given microstructure

In the case when the microstructural size is no longer negligible with respect to the characteristic length of the macroscopic deformation field a type of size effect may appear. This may occur due to a relatively small size of the macroscopic configuration (e.g. thin layers) or when localization of deformation takes place at the macrolevel. These size effects, which are generally associated with a dominant influence of the microstructure at the macrolevel, usually depend not only on the value and history of the strain tensor but also on its gradient. Classical continuum mechanics material models and, consequently, the first-order computational homogenization scheme, are not able to describe this size effect, since they do not incorporate a microstructural length scale. The second-order framework, on the other hand, is well capable to deal with these size effects, due to the account of the macroscopic gradient of the strain tensor [10]. This is illustrated in the following example.

Identical microstructural RVEs have been subjected to different tensile-bending macroscopic deformation histories. In these histories the strain tensor $\boldsymbol{\varepsilon}_M$ is the same, but its gradient $\boldsymbol{\eta}_M$, while representing the same deformation mode (bending), has different intensities. This has been achieved by a component-wise linear increase of the components of the prescribed $\boldsymbol{\eta}_M$. The resulting deformed RVEs are shown in Fig. 5.5. The left picture in Fig. 5.5 corresponds to the first-order case, not accounting for the strain gradient. Clearly, depending on the intensity of the strain gradient tensor, the overall deformation mode differs, which will result in different extracted overall responses, thereby capturing the size effect.

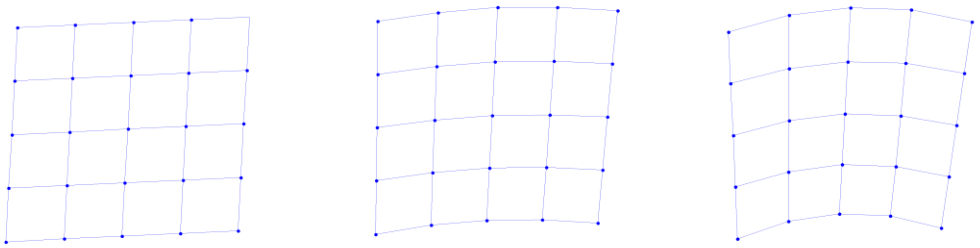

Figure 5.5: Dependence of the overall deformation mode on the intensity of the second-order strain. All the RVEs have been subjected to the same strain tensor $\boldsymbol{\varepsilon_M}$ and a gradient $\boldsymbol{\eta_M}$ of different intensity.

5.2 Modeling of pure bending

In this section, the micro–macro simulation algorithm has been verified on a pure bending problem.

For the macromodel we consider the cantilever beam shown in Fig 5.6. The geometrical properties are C = 10 mm, L = 60 mm, t = 5 mm and the concentrated force P=1000 N.

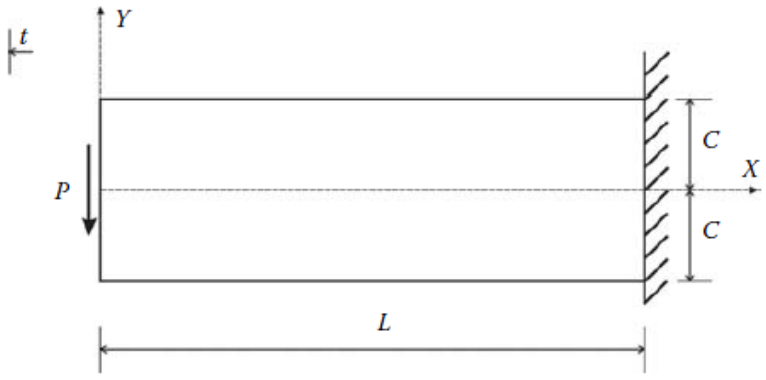

Figure 5.6: Cantilever beam in plane stress [9].

The macromodel is discretized by twenty four (24) C^1 triangular elements, as they were described in paragraph 3.3. The number of nodes are 21 and the nodes numbered 19, 20, and 21 represent the fixed end (Fig 5.7).

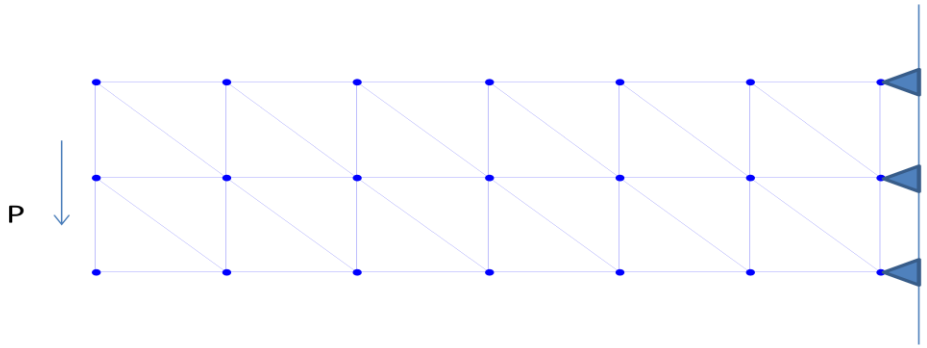

Figure 5.7: Finite element discretization with C^1 triangular elements.

The microscopic model (RVE) consisted of sixteen (16) quadrilateral elements, as it was shown in Fig 5.2.

The material data are the Young's modulus E = 200 GPa and the Poisson's ratio of ν= 0.3. Since the influence of the microfluctuation field for homogeneous materials is negligible, the displacements of the RVE boundary can be calculated by using displacement boundary conditions.

The deformed shape of the macromodel is presented in Fig. 5.8.

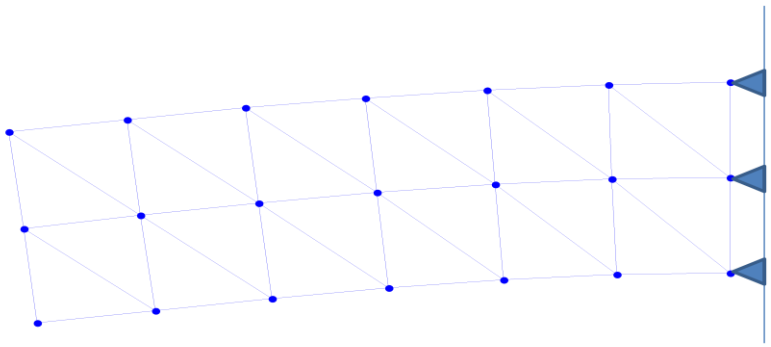

Figure 5.8: Deformed beam (Second-order scheme).

Comparing the deformed shape with results of standard FEM analysis (Fig 5.9) with the same number of elements and by using 3-nodes (linear) and 6-nodes (quadratic) triangular elements, we can see that the shape is acceptable.

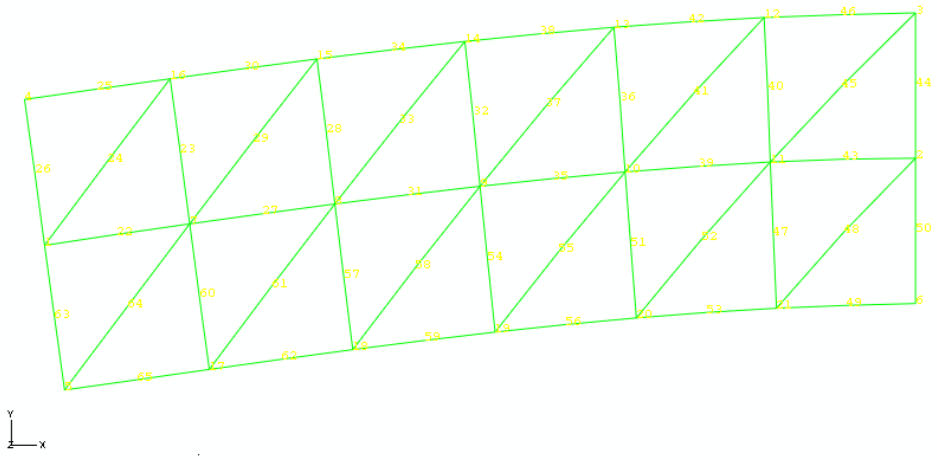

Figure 5.9: Deformed beam (FEM 6-nodes triangular elements).

Next we plot the vertical displacement of the nodes situated along the neutral axis of the cantilever (Fig.5.10). As it appears, a good correspondence is exhibited.

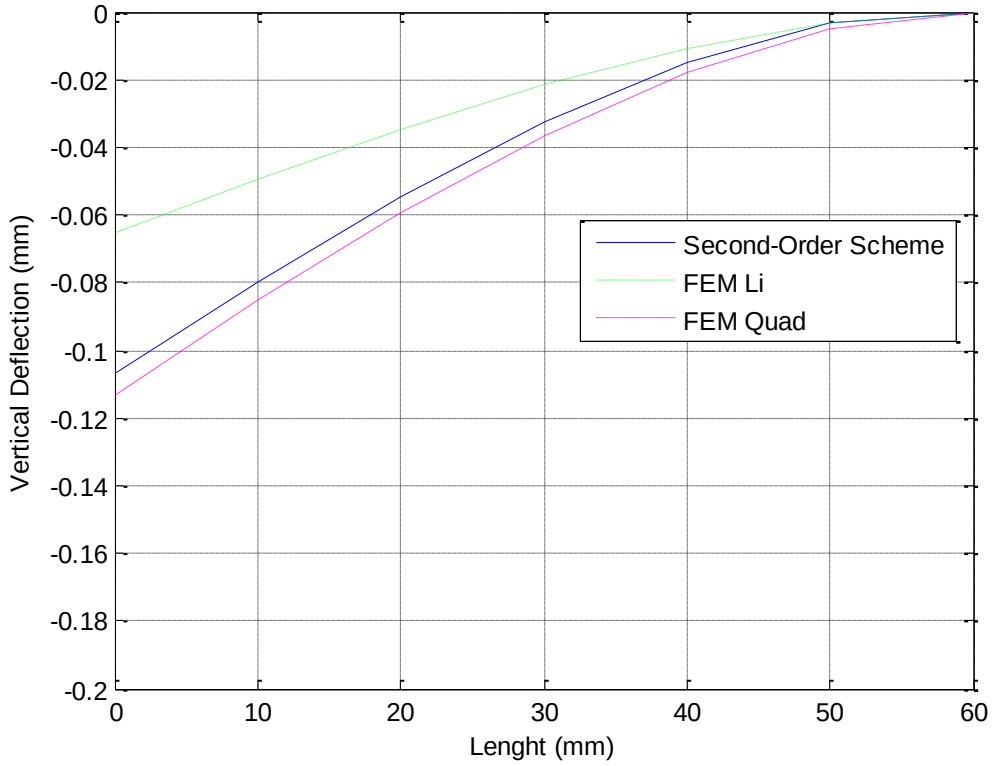

Figure 5.10: Deflection of the cantilever beam.

5.3 Linear Modelling

In this section, the cantilever beam problem of section 5.2, will be solved for the linear case of a non-homogeneous material using both the first-order and the second-order computational homogenization schemes.

5.3.1 Microscopic model

We consider a microstructure which consists of a fiber of diameter d_f=0.3568 (cross-section A_f=0.1), made of material with Young's modulus

E_f=1000, embedded in a matrix of thickness tm=1 and made of material with Young's modulus Em=100 and Poisson's ratio ν=0.2, which is represented by a RVE shown in Fig. 5.11.

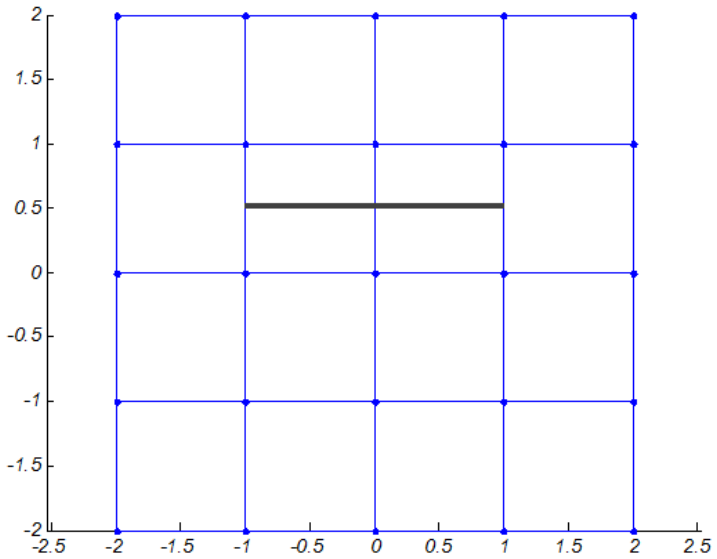

Figure 5.11: RVE with embedded fiber.

Full bond between the fiber and the matrix is assumed, that is, no slip is allowed between the two elements. The microstructure is modelled using plane-stress quadrilateral elements for the matrix. The model for full bond which has been used is that proposed by [14] (see Appendix B).

When the RVE is deformed monotonically with strain $\{\varepsilon_{11} \quad \varepsilon_{22} \quad 2\varepsilon_{12}\}^T = \{\varepsilon_1 \quad -0.2\varepsilon_1 \quad 0\}^T$, until strain ε_1=0.05 is achieved, and for $\boldsymbol{\eta_M}$=**0** using the first-order and second-order homogenization scheme, the response of averaging stress $\boldsymbol{\sigma_M}$ with prescribed strain is shown in Fig 5.12.

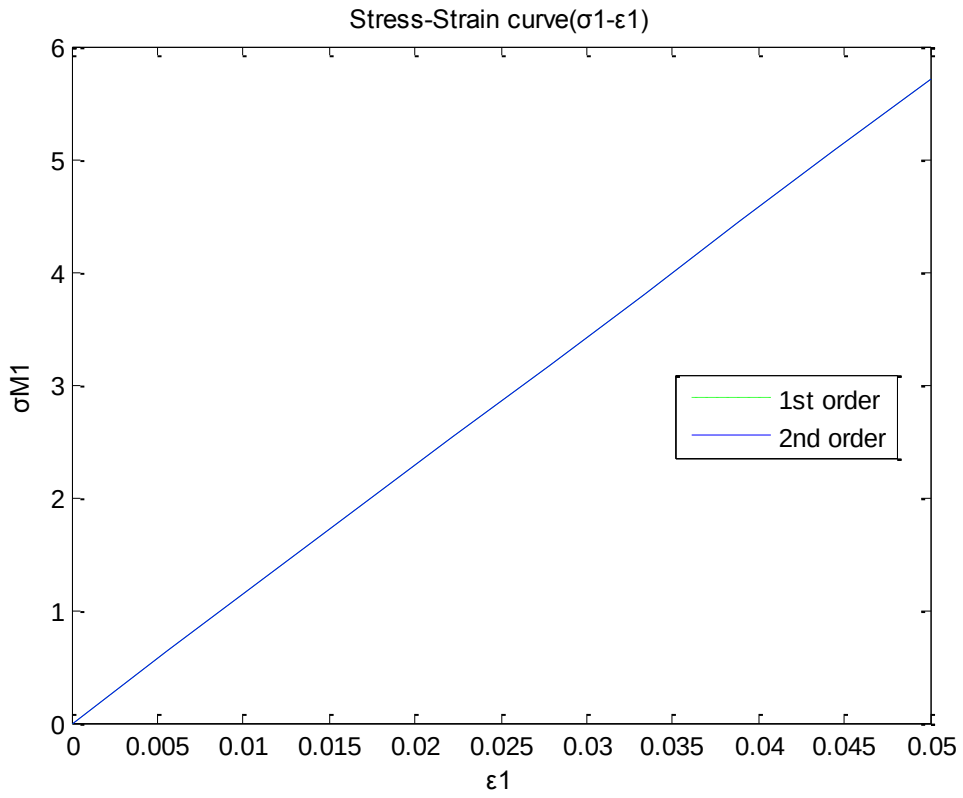

Figure 5.12: Averaging stress σ_{M11} -prescribed strain ε_1 response.

A we can see, for $\boldsymbol{\eta_M}$=**0** there is no difference between the two schemes.

5.3.2 Macroscopic model

For the macromodel we consider the cantilever beam described in section 5.2. The problem is solved with both the first-order and second-order homogenization scheme.

The first step is the initialization of the problem by partially solving the RVE to compute the constitutive matrices **C**. It is remarked that when the problem is linear, the homogenized macroscopic constitutive modulus can be computed once and used for all calculation steps at the macroscale. Since the matrices **C** are computed, the constitutive law is thus known for the macroscopic model. Macroscopic displacements, strains $\boldsymbol{\varepsilon_M}$ and strains gradients $\boldsymbol{\eta_M}$ can be obtain at every intergration point.

At the final stage the macroscale strains $\boldsymbol{\varepsilon_M}$ and strains gradients $\boldsymbol{\eta_M}$ are available and a postprocessing of the RVEs could be performed in order to find their stress and strains fields.

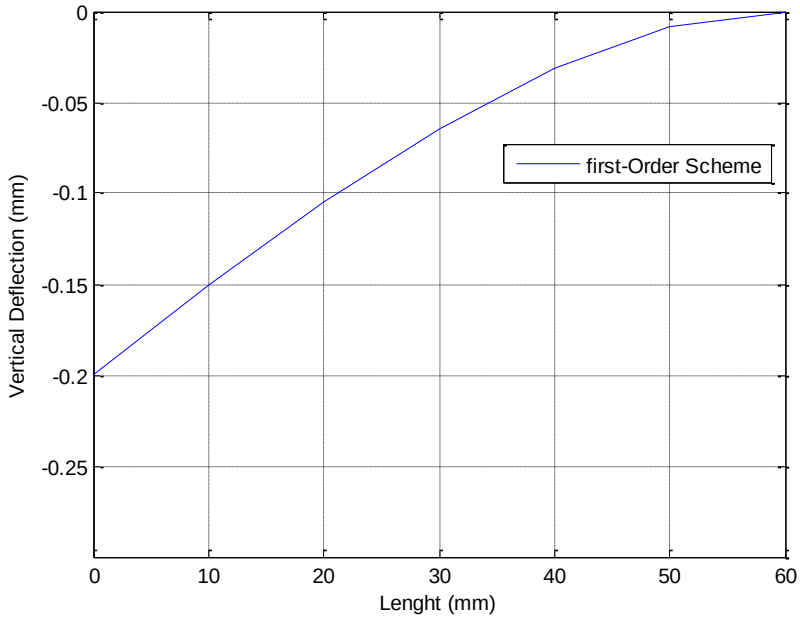

Figure 5.13: Vertical deflection of the neutral axis (First-order scheme).

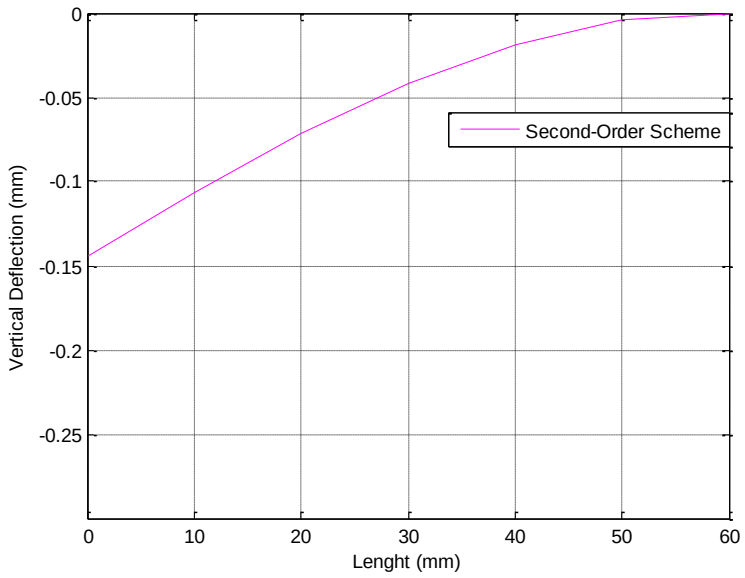

Figure 5.14: Vertical deflection of the neutral axis (Second-order scheme).

The vertical displacement of the nodes situated along the neutral axis of the cantilever for the solutions obtained by using the first-order and second-order homogenization schemes are depicted respectively on Fig. 5.13 and 5.14. As we notice the second-order scheme give us a stiffer response.

The stress distribution σ_{xx} of the macrolevel are presented in Fig. 5.15 and 5.16., portraying also the deformed shapes of RVEs in selected intergration points of the same area.

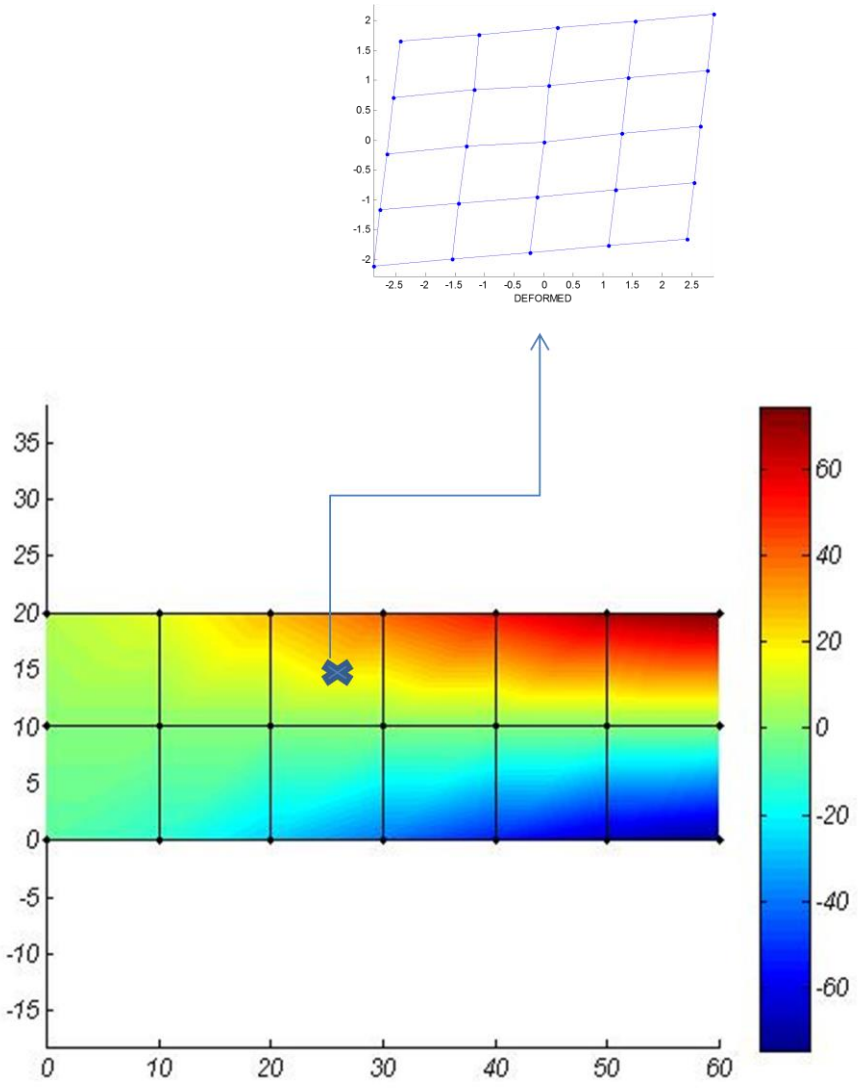

Figure 5.15: Stresses along the *x*-axis obtained with the first-order scheme.

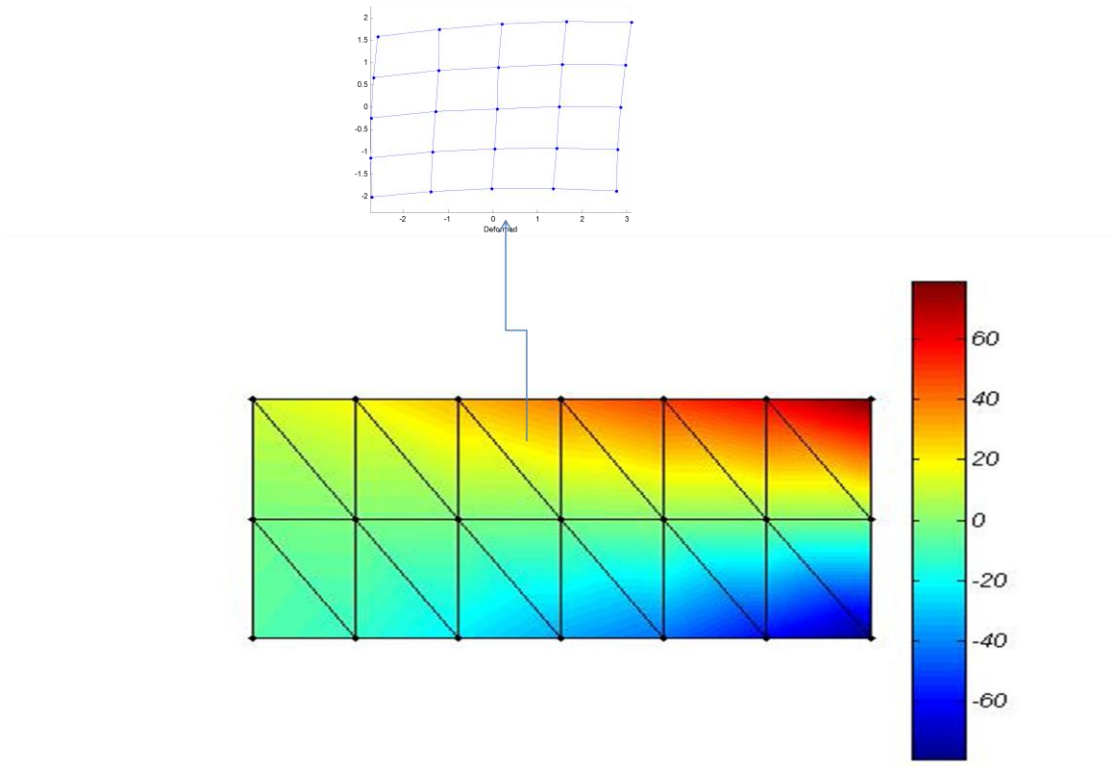

Figure 5.16: Stresses along the *x*-axis obtained with the second-order scheme.

Chapter 6

Conclusions

A wide range of manufactured, as well as natural, materials are heterogeneous at a certain scale of observation. If the heterogeneities are small compared to the scale of the whole problem, a standard finite element analysis often becomes computationally too large. For that reason various homogenization methods have been developed.

In the scope of this dissertation the two schemes, i.e the first-order and the second-order, of the computational multiscale homogenization method have been examined.

The computational multiscale homogenization method is based on the solution of nested boundary value problems, one for each scale. The most important characteristic of this solution strategy is that no constitutive assumptions are required on the macrolevel, since the macroscopic constitutive response is numerically obtained from the solution of a microscale boundary value problem.

The first-order computational homogenization scheme fits entirely in a standard local continuum mechanics framework. However, there are limitations in the application of the first-order scheme, because the size effects can not be neglected when considering problems of dimensions close to the characteristic length of the material.

In order to eliminate these limitations, the second-order computational homogenization procedure could be used. The second-order scheme is based on a proper incorporation of the macroscopic gradient of the strain tensor.

The second-order scheme algorithm have been programmed and implemented. According to the second-order formulation, the macrolevel was discretized by the C^1 triangular finite element based on the strain gradient

theory, while the standard C^0 quadrilateral was used for the discretization at the microlevel. The results for a bending problem of a homogeneous beam exhibited a good correspondence.

The second-order scheme was also compared with the first-order scheme in a bending problem. As it appears, the second-order scheme shows a stiffer behaviour.

It should also be mentioned, that, compared to the first-order framework, in the second-order computational homogenization the only additional computational effort is the solution of the higher-order equilibrium problem on the macrolevel, since the microstructural boundary value problem remains classical.

Moreover, the ability of the RVE within the second-order framework to capture differences of the macroscopic gradient was shown.

Bibliography

[1] Akarapu S. (2005). Numerical analysis of plane cracks in strain-gradient elastic materials. Master thesis, Washington State University.

[2] Akarapu S., Zbib HM (2006). Numerical analysis of plane cracks in strain-gradient elastic materials. Int J Fract 141:403–430.

[3] Dasgupta S., Sengupta D. (1990). A higher-order triangular plate bending element revisited. Int J Numer Meth Eng 30:419–430

[4] Drosopoulos G. A, Wriggers P., Stavroulakis G.E. (2014). A multi-scale computational method including contact for the analysis of damage in composite materials. Computational Materials Science 95, 522-535.

[5] Feyel, F. (2003). A multilevel finite element method (FE^2) to describe the response of highly non-linear structures using generalized continua. Elsevier.

[6] Geers M.G.D., Kouznetsova V.G., Brekelmans W.A.M. (2010). Multi-scale computational homogenization: Trends and challenges. Journal of Computational and Applied Mathematics 234, 2175-2182.

[7] Haukvik O. (2011) Computational Homogenization with Non-matching Grids treated with Localized Lagrange Multipliers. Master Thesis, Norwegian University of Science and Technology.

[8] Kaczmarczyk L., Pearce CJ, Bicanic N. (2008). Scale transition and enforcement of RVE boundary conditions in second-order computational homogenization. Int J Numer Methods Eng 74:506–522.

[9] Khennane A. (2013), Introduction to Finite Element Analysis Using MATLAB® and Abacus. CRC Press.

[10] Kouznetsova V. G. (2002). Computational homogenization for the multi-scale analysis of multi-phase materials. PhD. Thesis, Eindhoven University

[11] Kouznetsova V. G., Geers M.G.D., Brekelmans W.A.M. (2004). Multi-scale second-order computational homogenization of multi-phase materials: a nested finite element solution strategy. *Comput. Methods. Appl. Mech. Engrg.*, 193(48-51):5525–5550.

[12] Lesičar T., Tonković Z., Sorić J (2014). A second-order two-scale homogenization procedure using C_1 macrolevel discretization. Comp. Mech. DOI 10.1007.

[13] Luscher D. J. (2010), A Hierarchical framework for the multiscale modeling of microstructure evolution in heterogeneous materials. PhD Dissertation, Georgia Institute of Technology.

[14] Lykidis, G. C., & Spiliopoulos, K. V. (2008). 3D Solid Finite-Element Analysis of Cyclically Loaded RC Structures Allowing Embedded Reinforcement Slippage. *JOURNAL OF STRUCTURAL ENGINEERING* , 629-638.

[15] Miehe, C., & Koch, A. (2002). Computational micro-to-macro transitions of discretized microstructures undergoing small strains. *Springer-Verlag*, 300-317.

[16] Mindlin RD (1965). Second gradient of strain and surface-tension in linear elasticity. Int J Solids Struct 1:417–438.

[17] Shu JY, King WE, Fleck NA. (1999). Finite element for materials with strain gradient effects. Int J Numer Methods Eng 44,373‐91.

[18] Tavlaki M. (2013). Multiscale Finite Element Analysis. Postgraduate Dissertation, National Technical University of Athens.

[19] Toupin RA (1968) Elastic materials with couple stresses. Arch Ratio Mech Anal 11:385–413

[20] Zervos A, Papanicolopulos SA, Vardoulakis I (2009). Two finite element disretizations for gradient elasticity. J Eng Mech 135:203–213.

Appendix A

The shape functions of the C^1 triangular finite element used are [1]:

$$N_1 = L_1^5 + 5L_1^4L_2 + 5L_1^4L_3 + 10L_1^3L_2^2 + 10L_1^3L_3^2 + 20L_1^3L_2L_3 + 30r_{21}L_1^2L_2L_3^2 + 30r_{31}L_1^2L_3L_2^2$$

$$N_2 = c_3L_1^4L_2 - c_2L_1^4L_3 + 4c_3L_1^3L_2^2 - 4c_2L_1^3L_3^2 + 4(c_3 - c_2)L_1^3L_2L_3 - (3c_1 + 15r_{21}c_2)L_1^2L_2L_3^2 + \\ + (3c_1 + 15r_{31}c_3)L_1^2L_3L_2^2$$

$$N_3 = -b_3L_1^4L_2 + b_2L_1^4L_3 - 4b_3L_1^3L_2^2 + 4b_2L_1^3L_3^2 + 4(b_2 - b_3)L_1^3L_2L_3 + (3b_1 + 15r_{21}b_2)L_1^2L_2L_3^2 - \\ -(3b_1 + 15r_{31}b_3)L_1^2L_3L_2^2$$

$$N_4 = \frac{c_3^2}{2}L_1^3L_2^2 - \frac{c_2^2}{2}L_1^3L_3^2 - c_2c_3L_1^3L_2L_3 + (c_1c_2 + \frac{5}{2}r_{21}c_2^2)L_1^2L_2L_3^2 + (c_1c_3 + \frac{5}{2}r_{31}c_3^2)L_1^2L_3L_2^2$$

$$N_5 = -b_3c_3L_1^3L_2^2 - b_2c_2L_1^3L_3^2 + (b_2c_3 + b_3c_2)L_1^3L_2L_3 - (b_1c_2 + b_2c_1 + 5r_{21}b_2c_2)L_1^2L_2L_3^2 - \\ -(b_1c_3 + b_3c_1 + 5r_{31}b_3c_3)L_1^2L_3L_2^2$$

$$N_6 = \frac{b_3^2}{2}L_1^3L_2^2 + \frac{b_2^2}{2}L_1^3L_3^2 - b_2b_3L_1^3L_2L_3 + (b_1b_2 + \frac{5}{2}r_{21}b_2^2)L_1^2L_2L_3^2 + (b_1b_3 + \frac{5}{2}r_{31}b_3^2)L_1^2L_3L_2^2$$

where,

$$b_i = y_j - y_k$$

$$c_i = x_k - x_j$$

with *i*, *j*, *k* being cyclic permutations of 1,2 and 3.

$$r_{ij} = -\frac{b_i b_j + c_i c_j}{b_i^2 + c_i^2}$$

The remaining twelve components of the shape function, N_7 to N_{18}, corresponding to the degrees of freedom at nodes 2 and 3 are obtained by the cyclic permutations of the suffixes.

Appendix B

In this Appendix a brief summary of the model of full bond between fiber and matrix is presented, based on mathematical formulation of [14].

Let a fiber element be embedded in a "parent" matrix element, and let u_f be the displacement of the fiber, u_m the displacement of the matrix and s the slippage between the two (Fig. B.1).

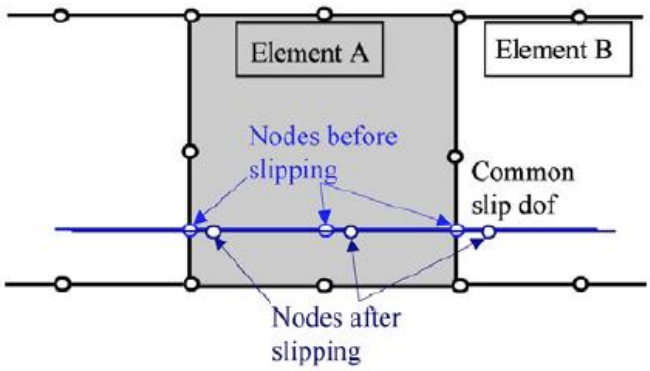

Figure B.1: [14]

In the case of full bond (i.e. no slippage), the virtual work principle is described by the system:

$$\left[\boldsymbol{K_{mm}} + \left(\sum_{i=1}^{nf} \boldsymbol{K_{ff,m,i}}\right)\right] \cdot \boldsymbol{\Delta d} = \boldsymbol{R_{t+\Delta t}} - \boldsymbol{Q_{m,f}}$$

where nf is the number of fibers embedded in the element, $\mathbf{R_t}$ are the external forces acting upon the matrix nodes and

$$\mathbf{K}_{ff,m} = \int_l \mathbf{B}_\mathbf{m}^\mathbf{T} \mathbf{T}^{*\mathbf{T}} E_f A_f \mathbf{T}^* \mathbf{B}_\mathbf{m} dl$$

$$\mathbf{K}_{\mathbf{mm}} = \int_{V_m} \mathbf{B}_\mathbf{m}^\mathbf{T} \mathbf{D}_\mathbf{m} \mathbf{B}_\mathbf{m} dV_m$$

$$\mathbf{Q}_{m,f} = \int_{V_m} \mathbf{B}_\mathbf{m}^\mathbf{T} \boldsymbol{\sigma}_\mathbf{m} dV_m + \int_l \mathbf{B}_\mathbf{m}^\mathbf{T} T^{*T} \boldsymbol{\sigma}_f A_f dl$$

$\mathbf{B_m}$ are the shape function derivatives for the parent matrix element,

$$\boldsymbol{T}^* = \{l_1^2 \quad m_1^2 \quad n_1^2 \quad l_1 \cdot n_1 \quad m_1 \cdot n_1 \quad l_1 \cdot n_1\}$$

with l_1, m_1, n_1 the direction cosines of the fiber,

V_m is the matrix volume, A_f the fiber section area, ℓ the fiber length, E_f the fiber Young's modulus and $\mathbf{D_m}$ the matrix constitutive matrix.